J. Fluid Mech. (2017), *vol.* 828, *pp.* 424–458.
doi:10.1017/jfm.2017.526

Statistics and structure of spanwise rotating turbulent channel flow at moderate Reynolds numbers

Geert Brethouwer†

Linné FLOW Centre and Swedish e-Science Research Centre, KTH Mechanics, SE-100 44 Stockholm, Sweden

(Received 8 November 2016; revised 27 July 2017; accepted 27 July 2017; first published online 4 September 2017)

A study of fully developed plane turbulent channel flow subject to spanwise system rotation through direct numerical simulations is presented. In order to study both the influence of the Reynolds number and spanwise rotation on channel flow, the Reynolds number $Re = U_b h/\nu$ is varied from a low 3000 to a moderate 31 600 and the rotation number $Ro = 2\Omega h/U_b$ is varied from 0 to 2.7, where U_b is the mean bulk velocity, h the channel half-gap, ν the viscosity and Ω the system rotation rate. The mean streamwise velocity profile displays also at higher Re a characteristic linear part with a slope near to 2Ω, and a corresponding linear part in the profiles of the production and dissipation rate of turbulent kinetic energy appears. With increasing Ro, a distinct unstable side with large spanwise and wall-normal Reynolds stresses and a stable side with much weaker turbulence develops in the channel. The flow starts to relaminarize on the stable side of the channel and persisting turbulent–laminar patterns appear at higher Re. If Ro is further increased, the flow on the stable side becomes laminar-like while at yet higher Ro the whole flow relaminarizes, although the calm periods might be disrupted by repeating bursts of turbulence, as explained by Brethouwer (*Phys. Rev. Fluids*, vol. 1, 2016, 054404). The influence of the Reynolds number is considerable, in particular on the stable side of the channel where velocity fluctuations are stronger and the flow relaminarizes less quickly at higher Re. Visualizations and statistics show that, at $Ro = 0.15$ and 0.45, large-scale structures and large counter-rotating streamwise roll cells develop on the unstable side. These become less noticeable and eventually vanish when Ro rises, especially at higher Re. At high Ro, the largest energetic structures are larger at lower Re.

Key words: rotating turbulence, turbulence simulation, turbulent flows

1. Introduction

Turbulent plane channel flow subject to rotation about the spanwise direction displays several phenomena of interest to engineering applications, turbulence modelling (Jakirlić, Hanjalić & Tropea 2002; Smirnov & Menter 2009; Arolla & Durbin 2013; Hsieh, Biringen & Kucala 2016) and subgrid-scale modelling in

† Email address for correspondence: geert@mech.kth.se

large-eddy simulation (Marstorp *et al.* 2009; Yang *et al.* 2012). Effects of rotation on flow and turbulence are in this case non-trivial. Channel flow is unaffected by rotation if fluid motions are two-dimensional and perpendicular to the rotation axis (Tritton 1992); for example, laminar Poiseuille flow and waves perpendicular to the rotation axis are not influenced (Brethouwer *et al.* 2014). Yet, it is well-established that spanwise rotation strongly influences Reynolds stresses, anisotropy and structures, and the mean velocity profile in plane turbulent channel flow (Johnston, Halleen & Lezius 1972). Rotation effects are therefore obviously related to three-dimensional turbulent processes.

A useful parameter when discussing rotation effects on turbulent shear flows is the ratio of background and mean shear vorticity. For a unidirectional shear flow with mean velocity $U(y)$ in the x-direction and shear vorticity $-\mathrm{d}U/\mathrm{d}y$ rotating with angular velocity Ω about the z-axis, this ratio is given by

$$S = -\frac{2\Omega}{\mathrm{d}U/\mathrm{d}y}. \tag{1.1}$$

When $S > 0$ the mean shear and background vorticity have the same sense of rotation and rotation is cyclonic, whereas when $S < 0$ they have the opposite sense and rotation is anticyclonic. Displaced particle analysis (Tritton 1992), rapid distortion theory, large-eddy and direct numerical simulation (DNS) of rotating homogeneous turbulent shear flow demonstrate that turbulence is damped if $S > 0$ and $S < -1$ and augmented if $-1 < S < 0$ (Salhi & Cambon 1997; Brethouwer 2005).

Experiments of fully developed turbulent plane channel flow subject to spanwise rotation by Johnston *et al.* (1972) at $Re = U_b h/\nu = 5750$, $Ro = 2\Omega h/U_b \leqslant 0.21$ and $Re = 17\,500$, $Ro \leqslant 0.081$, and by Nakabayashi & Kitoh (2005) at $Re \leqslant 2750$ and $Ro \leqslant 0.056$, where U_b is the bulk mean velocity, h channel half-width, ν viscosity and Ω rotation rate, have shown that turbulence is suppressed on one side of the channel where $S > 0$ and augmented on the other side where $-1 < S < 0$, in accordance with the discussion above. These sides are from now on called the stable and unstable side, respectively.

DNS of spanwise rotating channel flow have been carried out by Kristoffersen & Andersson (1993) at $Re_\tau = 194$ and $Ro \leqslant 0.5$, Lamballais, Lesieur & Métais (1996) at $Re = 2500$ and $Ro \leqslant 1.5$, Nagano & Hattori (2003) at $Re_\tau = 150$ and $Ro_\tau \leqslant 5$, corresponding to $Ro \lesssim 0.3$, and Liu & Lu (2007) at $Re_\tau = 194$ and $Ro_\tau \leqslant 7.5$, corresponding to $Ro \lesssim 0.5$. Here, Re_τ and Ro_τ are based on the friction velocity instead of U_b. Yang *et al.* (2012) have performed DNS of rotating channel flow at $Re = 7000$ and $Ro \leqslant 0.6$ to validate their large-eddy simulations. These DNS were broadly consistent with the experimental observations and show that at sufficiently high Ro the flow becomes laminar-like on the stable side owing to the strong suppression of turbulence. The asymmetry of the Reynolds stresses induces a skewed mean velocity profile and differences in the shear stresses on the two walls. Another notable feature is the appearance of a region in the channel where the mean velocity profile is linear with a slope $\mathrm{d}U/\mathrm{d}y \approx 2\Omega$, i.e. $S \approx -1$, implying that the absolute mean vorticity is nearly zero. Spanwise rotation also affects turbulence anisotropy since wall-normal fluctuations are typically strongly augmented on the unstable side (Kristoffersen & Andersson 1993), again in line with DNS of rotating homogeneous shear flow (Brethouwer 2005). Another consequence of spanwise system rotation is the emergence of large streamwise roll cells at certain values of Ro induced by the Coriolis force, as shown by experiments and DNS (Johnston *et al.* 1972; Kristoffersen & Andersson 1993; Dai, Huang & Xu 2016).

Higher Ro was considered by Grundestam, Wallin & Johansson (2008), who have performed DNS of spanwise rotating channel flow at $Re_\tau = 180$ and $Ro \leqslant 2.49$. Besides one-point statistics, they studied the effect of rotation on turbulent structures and Reynolds stress budgets. They observed that, at higher Ro, turbulence was also weak on the unstable side, suggesting that the flow fully relaminarizes at sufficiently high Ro. This can be understood from the fact that in Poiseuille flow $S \geqslant 0$ and $S \leqslant -1$ everywhere in the channel if $Ro \geqslant 3.0$. A more rigorous stability analysis shows that all modes with spanwise wavenumber $\beta \neq 0$ are linearly stable for $Ro > Ro_c$ in plane Poiseuille flow with spanwise rotation (Wallin, Grundestam & Johansson 2013). The critical rotation number Ro_c is a monotonic function of Re, i.e. $Ro_c = 2.80$ for $Re = 10\,000$ and $Ro_c \to 3.0$ for $Re \to \infty$. DNS confirms that the flow relaminarizes when $Ro \to Ro_c$ (Wallin *et al.* 2013).

However, Tollmien–Schlichting (TS) waves with a wave vector normal to the rotation axis are unaffected by spanwise rotation and become linearly unstable in plane Poiseuille flow if $Re \geqslant 3848$ (Schmid & Henningson 2001). DNS indeed reveal TS wave instabilities resulting in a continuous cycle of turbulent bursts if $Ro \simeq Ro_c$ and the flow is basically laminar (Wallin *et al.* 2013). However, absence of turbulence is not a prerequisite for TS instabilities, as shown by Brethouwer *et al.* (2014), who have observed cyclic bursts of intense turbulence triggered by an unstable TS wave in DNS at $Re = 20\,000$ and $Ro = 1.2$ when turbulence is strong on the unstable side. An extensive study of DNS of spanwise rotating channel flow reveals that these cyclic turbulent bursts and TS wave instabilities show up in a quite wide range of Re and Ro, including cases with overall weak turbulence as well as strong continuous turbulence on the unstable side (Brethouwer 2016). The observed TS instability growth was compared with the predictions of linear stability theory and analysed in detail.

DNS at $Re_\tau = 180$ and a wide range of Ro were also performed by Xia, Shi & Chen (2016). They studied various one-point statistics and observed a linear part in the profile of the streamwise Reynolds stress production at sufficiently high Ro. Another study of spanwise rotating channel flow was performed by Yang & Wu (2012), who have carried out DNS at $Re_\tau = 180$ and performed a helical wave decomposition. This shows that at low Ro, energy concentrates in large-scale modes, presumably streamwise roll cells, while at higher Ro, energy accumulates at smaller scales. In DNS with periodic boundary conditions these roll cells appear as pairs of counter-rotating vortices. Dai *et al.* (2016) have detected roll cells, sometimes called Taylor–Görtler vortices, in DNS at $Re = 2800$ and $0.1 \leqslant Ro \leqslant 0.5$ and $Re = 7000$ and $Ro = 0.3$, and studied their effect on the turbulence. They found that, somewhat counter-intuitively, turbulence is enhanced on the unstable side in the low-wall-shear-stress region where the fluid is pumped away from the wall by the counter-rotating roll cells. Hsieh and Biringen have carried out DNS of rotating channel flow at $Re_\tau \approx 200$ with $0 \leqslant Ro \leqslant 0.5$ and $Re_\tau \approx 400$ with $Ro = 0.2$ with varying domain sizes. At low Re_τ they observed that when the spanwise domain was too small to capture a full pair of counter-rotating roll cells, the mean velocity profiles and Reynolds stresses were incorrect, illustrating that the roll cells have a significant impact on the momentum transfer and turbulence. At higher Re_τ, the mean velocity and Reynolds stresses changed significantly when the spanwise domain size was reduced from $2\pi h$ to πh.

These previous studies of spanwise rotating channel flow were mostly limited to low Reynolds numbers, $Re_\tau \leqslant 194$, meaning that the influence of the Reynolds number on the statistics, turbulent structures and relaminarization on the stable side can be

significant. Exceptions are the experiments of Johnston *et al.* (1972) and DNS of Dai *et al.* (2016) and Hsieh & Biringen (2016) at somewhat higher Re, albeit limited to moderate Ro. It is therefore not completely clear if the previous observations have been influenced by the low Re. I have carried out DNS of plane turbulent channel flow subject to spanwise rotation at higher Reynolds numbers than in previous studies with Re up to 31 600 and a wide range of Ro. My aim is to assess the influence of spanwise rotation on the mean velocity, one-point statistics and Reynolds stress budgets at these higher Re. With these simulations I will investigate whether the effects of rotation on the mean flow and turbulence discussed above are either generic or influenced by the Reynolds number. Another goal is to study the relaminarization of the flow on the stable channel side at high Ro and turbulence structures, and examine if roll cells exist in rotating channel flow at these higher Re. Some previous observations of the flow structures and relaminarization may have been affected by the limited computational domains that were often used in the numerical studies. In the present study, I therefore use larger computational domains and study the structures through visualizations, two-point correlations and spectra. Finally, the effect of Re on the flow statistics and structures is studied at a fixed Ro. The present study is also motivated by the need for higher-Re data of rotating channel flow for turbulence modelling.

2. Numerical method and parameters

The velocity $\boldsymbol{u}$ in the DNS is governed by the incompressible Navier–Stokes equations

$$\frac{\partial \boldsymbol{u}}{\partial t} + \boldsymbol{u}\cdot\boldsymbol{\nabla}\boldsymbol{u} = -\boldsymbol{\nabla}p + \frac{1}{Re}\nabla^2\boldsymbol{u} - Ro(\boldsymbol{e}_z \times \boldsymbol{u}), \quad \boldsymbol{\nabla}\cdot\boldsymbol{u} = 0, \tag{2.1}$$

where $\boldsymbol{e}_z$ is the unit vector in the z-direction and p the pressure, including the centrifugal acceleration. The equations are non-dimensionalized by the mean bulk velocity U_b and channel half-gap h; time t is thus given in terms of a convection time h/U_b. Streamwise, wall-normal, spanwise coordinates are denoted by x, y, z, respectively, and boundary conditions are periodic in the streamwise and spanwise directions and no-slip at the walls. A sketch of the geometry is shown in Brethouwer (2016). In the present DNS $y=-1$ and 1 correspond to the wall on the unstable and stable channel side, respectively.

Equations (2.1) are solved with a pseudo-spectral code with Fourier expansions in the homogeneous x- and z-direction and Chebyshev polynomials in the y-direction (Chevalier *et al.* 2007), and the spatial resolution is similar to in previous channel flow DNS (Lee & Moser 2015). In all runs, the flow rate and thus Re was kept constant by adapting the mean pressure gradient. Re is varied from 3000 up to 31 600 and Ro from 0 (non-rotating) to approximately Ro_c, which is between 2.67–2.87 for this range of Re. In most DNS, the streamwise and spanwise domain size are either $12\pi h \times 10.5h$ or $8\pi h \times 3\pi h$, but in some DNS the domain size was chosen differently to accommodate TS instabilities, as explained in Brethouwer (2016), but this variation has little effect on results presented here. The runs are sufficiently long to reach a statistically stationary state in all DNS. Parameters of the DNS at $Re = 3000$–$31\,600$ are listed in table 1. The friction velocity is calculated as $u_\tau = [u_{\tau u}^2/2 + u_{\tau s}^2/2]^{1/2}$, where $u_{\tau u}$ and $u_{\tau s}$ are the friction velocity of unstable and stable channel side, respectively (Grundestam *et al.* 2008). With this definition the mean dimensional pressure gradient $\partial P/\partial x = \rho u_\tau^2/h$, where ρ is the fluid density. Re_τ^u and Re_τ^s are Reynolds numbers based on $u_{\tau u}$ and $u_{\tau s}$, respectively, and $Ro_\tau = 2\Omega h/u_\tau$. The DNS studied here are basically the same as those reported in Brethouwer (2016).

Re_b	Ro	Re_τ	Re_τ^u	Re_τ^s	Ro_τ	$L_x/h \times L_z/h$	$N_x \times N_y \times N_z$
31 600	0	1505	1505	1505	0	$12\pi \times 10.5$	$6144 \times 577 \times 3456$
31 600	0.45	1213	1445	925	11.7	$12\pi \times 10.5$	$4608 \times 481 \times 2560$
31 600	0.9	822	988	613	34.6	$12\pi \times 10.5$	$3072 \times 385 \times 1728$
31 600	1.2	562	670	428	67.4	$12\pi \times 10.5$	$2048 \times 257 \times 1152$
30 000	1.5	415	462	363	108	$8\pi \times 3\pi$	$1024 \times 193 \times 768$
30 000	2.1	319	318	319	198	$8\pi \times 4.8\pi$	$864 \times 161 \times 864$
30 000	2.4	302	306	298	238	$8\pi \times 3\pi$	$640 \times 193 \times 512$
30 000	2.7	301	302	300	269	$7.5\pi \times 3\pi$	$432 \times 161 \times 384$
20 000	0	1000	1000	1000	0	$8\pi \times 3\pi$	$2560 \times 385 \times 1920$
20 000	0.15	976	1107	825	3.1	$8\pi \times 3\pi$	$2304 \times 385 \times 1728$
20 000	0.45	800	964	594	11.2	$8\pi \times 3\pi$	$2048 \times 361 \times 1536$
20 000	0.65	700	851	505	18.6	$8\pi \times 3\pi$	$1920 \times 321 \times 1440$
20 000	0.9	544	677	365	33.1	$8\pi \times 3\pi$	$1536 \times 257 \times 1152$
20 000	1.2	423	501	326	56.7	$8\pi \times 3\pi$	$1152 \times 217 \times 864$
20 000	1.5	333	370	292	90.0	$29.4 \times 4\pi$	$864 \times 193 \times 768$
20 000	2.1	259	265	252	162	$8\pi \times 3\pi$	$512 \times 161 \times 432$
10 000	0	544	544	544	0	$8\pi \times 3\pi$	$1152 \times 193 \times 864$
10 000	0.45	435	535	304	10.3	$8\pi \times 3\pi$	$1024 \times 193 \times 768$
10 000	0.9	339	416	240	26.5	$8\pi \times 3\pi$	$768 \times 161 \times 576$
10 000	1.2	277	325	219	43.3	$8\pi \times 3\pi$	$576 \times 129 \times 432$
10 000	1.5	226	249	199	66.5	$16\pi \times 6\pi$	$1280 \times 161 \times 960$
10 000	1.8	196	207	185	91.6	$16\pi \times 6\pi$	$1024 \times 129 \times 768$
10 000	2.1	182	186	178	115	$16\pi \times 6\pi$	$640 \times 129 \times 512$
5 000	0	297	297	297	0	$8\pi \times 3\pi$	$576 \times 109 \times 432$
5 000	0.15	277	326	217	2.7	$8\pi \times 3\pi$	$576 \times 109 \times 432$
5 000	0.45	251	310	174	8.9	$8\pi \times 3\pi$	$512 \times 109 \times 384$
5 000	0.9	214	258	159	21.0	$8\pi \times 3\pi$	$432 \times 109 \times 320$
5 000	1.2	182	211	148	32.9	$8\pi \times 3\pi$	$384 \times 97 \times 288$
5 000	1.5	154	170	137	48.6	$8\pi \times 3\pi$	$320 \times 97 \times 240$
5 000	1.8	137	144	129	65.8	$27 \times 3\pi$	$288 \times 97 \times 216$
5 000	2.1	128	130	125	82.2	$8\pi \times 3\pi$	$256 \times 97 \times 192$
3 000	0	190	190	190	0	$8\pi \times 3\pi$	$320 \times 97 \times 256$
3 000	0.15	179	213	138	2.5	$8\pi \times 3\pi$	$320 \times 97 \times 256$
3 000	0.45	174	211	127	7.8	$8\pi \times 3\pi$	$320 \times 97 \times 256$
3 000	0.9	153	181	118	17.7	$8\pi \times 3\pi$	$256 \times 97 \times 216$
3 000	1.2	134	154	112	26.8	$8\pi \times 3\pi$	$216 \times 97 \times 180$
3 000	1.5	117	128	105	38.6	$8\pi \times 3\pi$	$192 \times 97 \times 144$

TABLE 1. DNS parameters: N_x, N_y and N_z are the number of modes in the streamwise, wall-normal and spanwise direction, and L_x and L_z, are the streamwise and spanwise computational domain size, respectively.

3. Flow visualizations

Before discussing flow statistics and spectra, visualizations are presented to get an understanding of the main flow characteristics. In all following two-dimensional visualizations the complete domain is shown. Figure 1(*a–d*) shows plots of the instantaneous streamwise velocity in an x–z plane close to wall on the stable side at $Re = 31\,600$ and $Ro \leqslant 1.2$. Structures with a width of $O(h)$ are vaguely visible

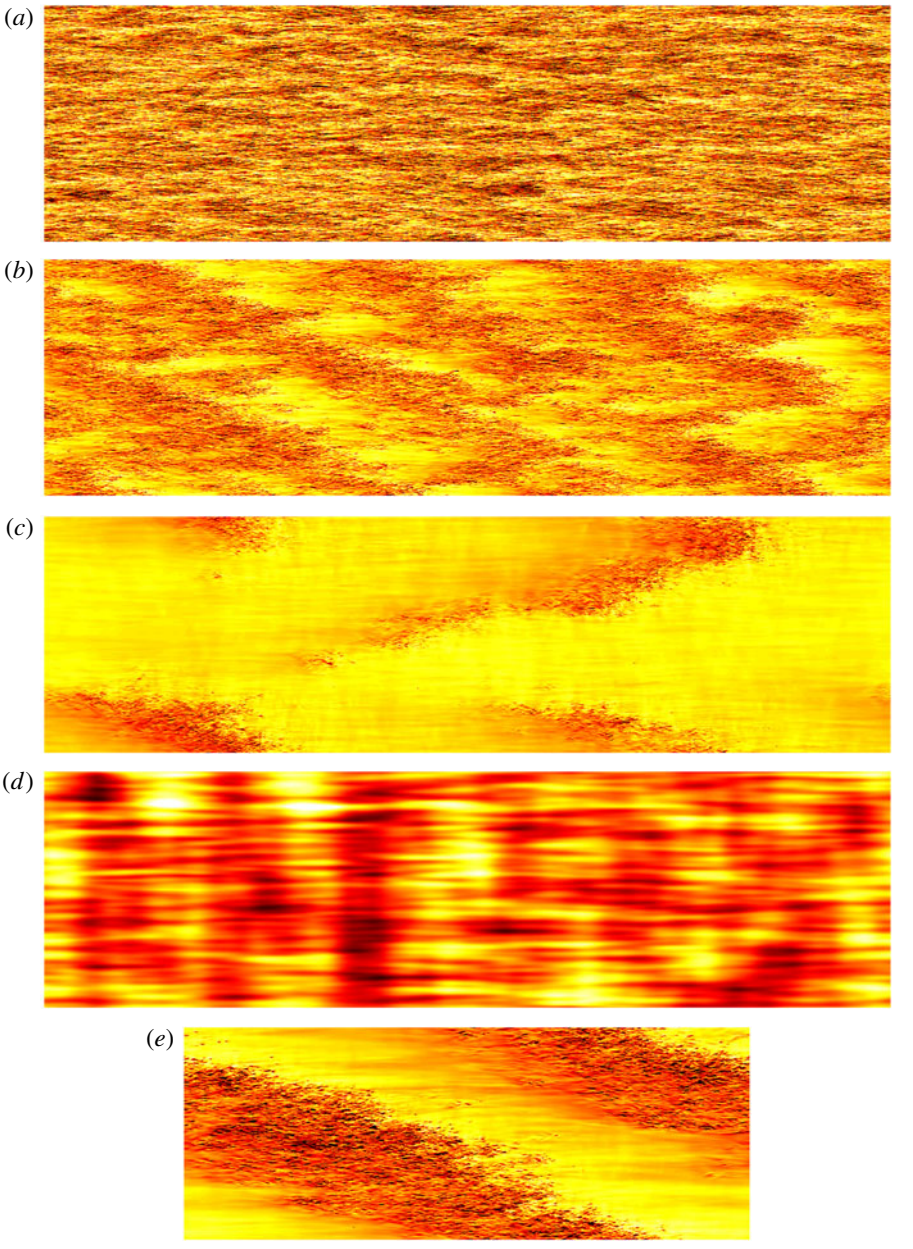

FIGURE 1. (Colour online) Visualizations of the instantaneous streamwise velocity in an x–z plane at $y^+ \approx 5$ on the stable channel side. Dark colours signify high velocities. $Re = 31\,600$ and (*a*) $Ro = 0$, (*b*) $Ro = 0.45$, (*c*) $Ro = 0.9$, (*d*) $Ro = 1.2$. (*e*) $Re = 20\,000$ and $Ro = 0.45$.

at $Ro = 0$ (figure 1*a*), indicating near-wall turbulence modulation by large-scale outer structures (Mathis, Hutchins & Marusic 2009). In rotating channel flow, turbulence becomes progressively weaker on the stable side with increasing rotation speeds. At low rotation rates, the flow is fully turbulent on the stable side, but at

$Ro = 0.45$ it is no longer fully turbulent and regions with small-scale turbulence as well as regions where turbulence is mostly absent can be seen in figure 1(*b*). The regions with small-scale turbulence have a weakly visible oblique band-like structure with an angle of approximately 30° to the flow direction. Similar oblique patterns have been observed in, for example, transitional plane Couette flow (Barkley & Tuckerman 2007; Duguet, Schlatter & Henningson 2010) as well as in other flows with some stabilizing force like stratified open channel flow, magnetohydrodynamic channel flow and rotating Couette flows (Brethouwer, Duguet & Schlatter 2012) and stratified Ekman layers (Deusebio *et al.* 2014). In rotating channel flow the turbulent–laminar patterns exist only on the stable side since the other side is fully turbulent. The turbulent–laminar patterns are not transitional but persist in time, like in the aforementioned studies.

When Ro is raised to 0.9 the turbulent fraction becomes smaller and the turbulent regions appear as spots and bounded band-like oblique structures (figure 1*c*), while at $Ro = 1.2$ and higher no small-scale turbulence is present and only weak larger-scale fluctuations are seen on the stable channel side (figure 1*d*). In the latter case, a continuous cycle of strong turbulent bursts with a long period of $O(1000h/U_b)$ on the stable side occurs caused by a linear TS wave instability (Brethouwer 2016) and a vague imprint of the TS wave is visible in figure 1. At other times the TS wave is often more prominent.

At a lower $Re = 20\,000$ the flow is fully turbulent on the stable channel side at $Ro = 0.15$ (shown later), whereas at $Ro = 0.45$ one distinct oblique turbulent and laminar banded pattern can be observed (figure 1*e*). At the same Ro, but a higher $Re = 31\,600$ in a DNS with a larger domain, turbulent–laminar patterns are more numerous but less explicit (figure 1*b*). Although the angle of the oblique pattern in figure 1(*e*) is determined by the periodic boundary conditions and the domain size, it is similar to the angle of the patterns seen in figure 1(*b*,*c*) and the oblique patterns in other flow cases (Duguet *et al.* 2010; Brethouwer *et al.* 2012). Duguet & Schlatter (2013) argue that the obliqueness of the patterns is caused by a large-scale flow with a non-zero spanwise velocity. In previous DNS of rotating channel flow discussed in the Introduction, such patterns have not been observed, which is likely owing to the use of fairly limited computational domains.

However, in a certain Re–Ro range Johnston *et al.* (1972) observed laminar flows interspersed with turbulent spots on the stable channel side in their experiments, confirming that such transitional flows are found at lower Ro and Re. In DNS at $Re = 7000$ and $Ro = 0.3$, Dai *et al.* (2016) observed quasi-periodic behaviour of the wall shear stress and turbulence intensity on the stable side because the flow continuously alternated between laminar-like and intermittent with large-scale streamwise bands with either turbulent or laminar features. They attributed this quasi-periodic behaviour to the dynamics of the streamwise roll cells in their DNS. Streamwise turbulent–laminar bands, as observed by Dai *et al.* (2016), are not seen in the present DNS, which may be related to the size of the computational domain. On the other hand, strong quasi-periodic variations of the wall shear stress and turbulence intensity are observed in some of the present DNS, but these were caused by a linear instability of a TS-like wave, as explained in Brethouwer (2016). This quasi-periodic behaviour is not observed in all but one DNS without this linear instability. The exception is the DNS at $Re = 10\,000$ and $Ro = 0.45$, where large variations of approximately 30 % are seen in the wall shear stress on the stable channel side. Visualizations (not shown here) reveal that these variations are related to quasi-periodically growing and decaying turbulent spots on this side. When

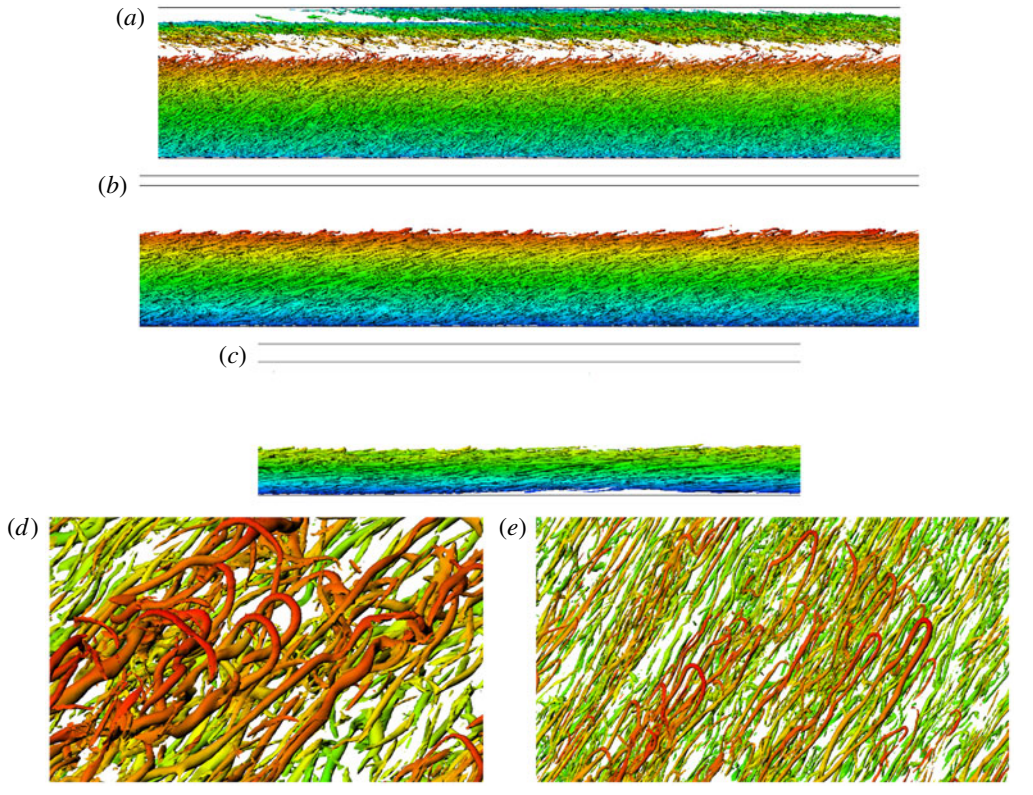

FIGURE 2. (Colour online) Isocontours of (*a*) $\lambda_2 = -9$ at $Re = 31\,600$ and $Ro = 0.9$, (*b*) $\lambda_2 = -2.25$ at $Re = 31\,600$ and $Ro = 1.2$, (*c*) $\lambda_2 = -0.45$ at $Re = 30\,000$ and $Ro = 2.1$ (side views, stable channel side is at the top) and close up at isocontours of (*d*) $\lambda_2 = -5.6$ at $Re = 31\,600$ and $Ro = 0.9$, (*e*) $\lambda_2 = -2.25$ at $Re = 31\,600$ and $Ro = 1.2$. The isosurfaces are coloured with streamwise velocity. The velocity increases from blue to red.

the wall shear stress reaches a minimum, the spots almost disappear. Large cyclic variations in the wall shear stress have also been observed in DNS of transitional strongly stratified channel and plane Couette flows (Garcia-Villalba & del Álamo 2011; Deusebio, Caulfield & Taylor 2015), but these variations disappeared when the computational domain was enlarged, indicating that this behaviour is strongly affected by the size of domain. DNS of spanwise rotating channel flow by Hsieh & Biringen (2016) confirm that the intermittency on the stable channel side can be strongly influenced by the computational domain size when the flow is transitional there.

Continuing with the present cases, if $Ro \geqslant 0.9$ and $Re = 20\,000$ or lower, no turbulent spots or band-like structures are seen like in figure 1(*c*), illustrating that Re effects can be appreciable, as discussed in more detail later. Only weak larger-scale fluctuations are observed on the stable side at high Ro, as illustrated in figure 1(*d*). However, in a number of cases the calm periods on the stable side are interrupted by violent bursts of turbulence triggered by a linear instability, as explained before.

Figure 2 shows λ_2 isocontours at three different Ro (Jeong & Hussain 1995) coloured with the streamwise velocity to identify vortices. The strongly turbulent unstable side of the channel with intense vortices obviously shrinks with Ro. Between

the unstable side with strong turbulence, and clearly identifiable vortices and stable side with weak turbulence, a seemingly sharp and flat border exists (figure 2*a–c*), as was noted by Johnston *et al.* (1972), although when $Ro = 0.9$ some areas with vortices corresponding to the patterns in figure 1(*c*) can still be seen on the stable side. Rotation promotes the formation of streamwise vortices on the unstable side (Dai *et al.* 2016), especially in the region where the absolute mean vorticity is approximately zero (Lamballais *et al.* 1996). Indeed, close ups of the vortices on the border between the unstable and stable channel side at $Ro = 0.9$ and 1.2 in figure 2(*d*,*e*) reveal elongated streamwise vortices and, remarkably, packages of hairpin vortices which are detached from the wall. The red colour signifies that hairpin vortices are mostly found near the streamwise velocity maximum on the border between the unstable and stable channel side. At higher Ro, vortices including the head of the hairpin vortices become increasingly aligned with the streamwise direction, and hairpin vortices, as discussed by Adrian (2007), become less explicitly visible (not shown here). Yang & Wu (2012) argued that the Coriolis force reduces the inclination angle of the vortices and favours their streamwise elongation on the unstable side, whereas on the stable channel side this force impedes this streamwise elongation. Lamballais *et al.* (1996) observed that vortices become aligned with the flow direction with Ro, and remarked that, especially in the region where the absolute mean vorticity is approximately zero, streamwise vortex stretching is promoted. These findings are broadly consistent with the present visualizations.

Large, steady streamwise roll cells induced by the Coriolis force have been observed on the unstable side in several experimental and numerical studies of rotating channel flow (Dai *et al.* 2016). Steady means here that they have a relatively long lifetime, although in the experiments of Johnston *et al.* (1972) the roll cells changed in time, whereas in a DNS by Kristoffersen & Andersson (1993) they were more coherent and stationary at $Ro = 0.15$ and spanned the whole channel.

Visualizations of the instantaneous wall-normal velocity field in the present DNS are shown in figure 3. Narrow elongated streaks with positive wall-normal velocity away from the wall in a wall parallel x–z plane on the unstable side (figure 3*a*) and regions with alternating positive and negative wall-normal velocity in a cross-stream y–z plane at $Ro = 0.15$ and $Re = 20\,000$ (figure 3*d*) indicate the presence of large streamwise roll cells on the unstable side that extend up to the border between the unstable and the stable side. The structures are long, but not as coherent as in the DNS by Kristoffersen & Andersson (1993) since they appear to break up or split at some places. Possible reasons for the reduced coherency can be the higher Re and the larger computational domain in the present study, which puts fewer constraints on the dynamics of the structures through the periodic boundary conditions.

The clustering of intense vortices in streamwise near-wall streaks seen in figure 3(*g*) show that the roll cells modulate the near-wall dynamics on the unstable side. Dai *et al.* (2016) observed in their DNS of spanwise rotating channel flow that turbulence and vortices on the unstable side are stronger in the regions where the fluid is pumped away from the wall by the counter-rotating roll cells and the local mean wall shear stress has a minimum, but this augmentation was weaker at a higher Re. The higher vorticity was found to be caused by the Coriolis term and strong vortex stretching. This apparently contrasts the effect of large-scale motions in non-rotating wall flows. Experiments by Talluru *et al.* (2014) suggest the presence of large-scale counter-rotating vortices in turbulent boundary layer flow. They show that turbulence is weaker in the near-wall regions, where the fluid is pumped away from the wall by these vortices and the local wall shear stress has a minimum, and stronger where the

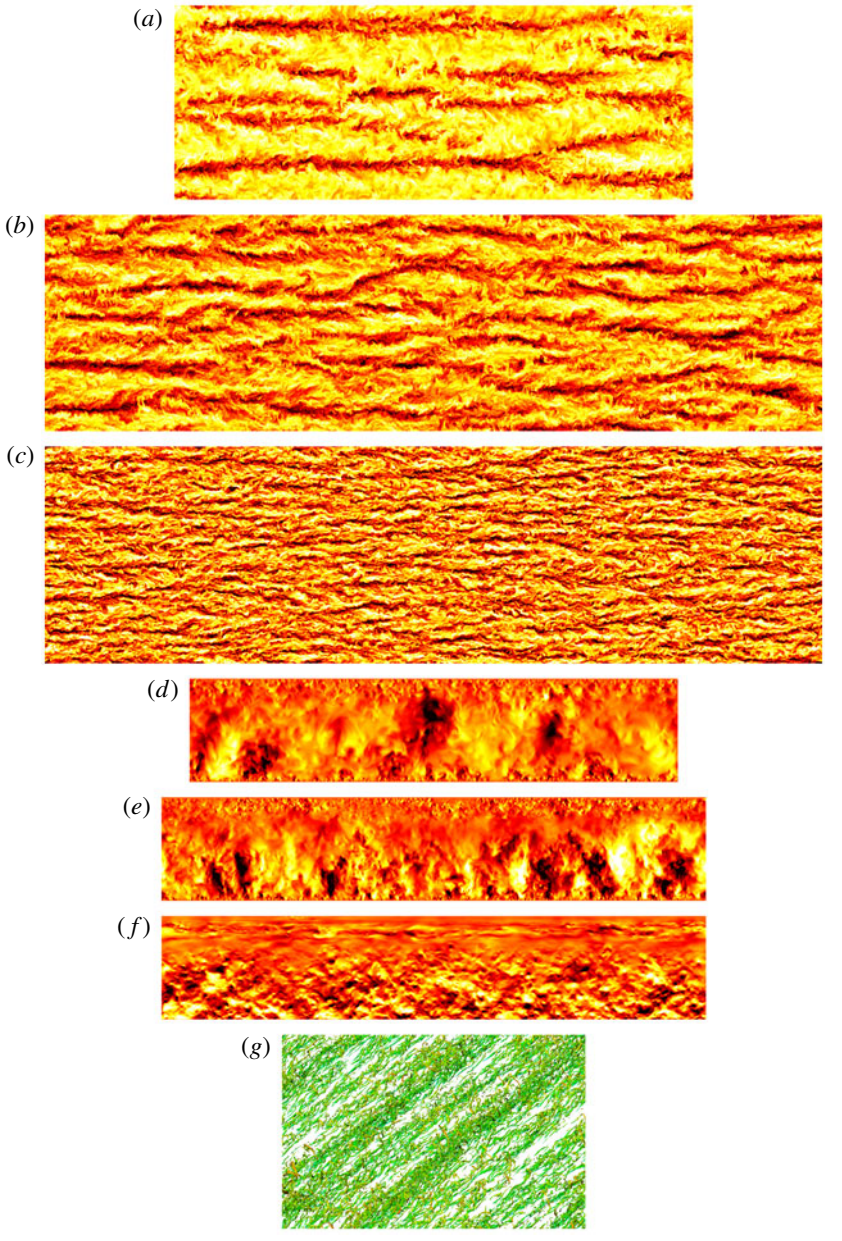

FIGURE 3. (Colour online) Visualizations of the instantaneous wall-normal velocity in an x–z plane (a) at $y=-0.5$ and $Re=20\,000$, $Ro=0.15$, (b) at $y=-0.5$ and $Re=31\,600$, $Ro=0.45$, (c) at $y=-0.75$ and $Re=31\,600$, $Ro=0.9$ and in a y–z plane at (d) $Re=20\,000$, $Ro=0.15$, (e) $Re=31\,600$, $Ro=0.45$, (f) $Re=31\,600$, $Ro=0.9$. Dark colours signify positive velocities. (g) Isocontours of $\lambda_2=-36$ at $Re=20\,000$ and $Ro=0.15$ near the wall on the unstable side. The flow is from bottom left to upper right corner.

large-scale motions induce a high wall shear stress, in agreement with Agostini & Leschziner (2016). The different effect of large-scale motions in non-rotating versus rotating wall flows is presumably a result of the Coriolis term, which affects both

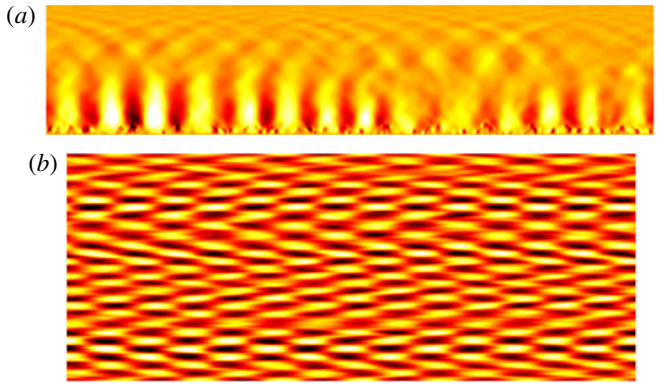

FIGURE 4. (Colour online) Visualization of the instantaneous wall-normal velocity for $Re = 30\,000$ and $Ro = 2.7$ in a (a) y–z plane and in an (b) x–z plane at $y = -0.8$. Colour scale ranges from $v = -0.021$–0.021 in (b).

the Reynolds stresses and vorticity. Roll cells in rotating flows are likely also more coherent and steady, and induce stronger wall-normal velocities.

Streaks with positive wall-normal velocity (figure 3b) and large-scale regions with positive and negative wall-normal velocity (figure 3e) at $Ro = 0.45$ and $Re = 31\,600$ indicate roll cells, but they seem to be smaller and less coherent than at $Ro = 0.15$. Streaky structures with a positive wall-normal velocity are also seen in figure 3(c) in the DNS at $Ro = 0.9$, but it is not clear if these upward and downward motions seen in figure 3(f) can be interpreted as signs of roll cells. The spacing and form of the streaks indicate that the roll cells, if they exist, are smaller and less coherent than at lower Ro. Roll cells also became smaller in the DNS of rotating channel flow at $Re = 2800$ by Dai *et al.* (2016) when Ro was raised from 0.1 to 0.5. Signs of roll cells are visible in the DNS at $Ro = 0.45$ and 0.9, but for lower Re (not shown here). When $Ro = 1.2$ or higher, no visible signs of roll cells are found at $Re = 20\,000$ and 31 600. However, at $Re = 5000$, visualizations hint at the existence of roll cells, and Grundestam *et al.* (2008) observed them at $Ro = 1.27$ and $Re_\tau = 180$. These observations suggest that, at lower Re, roll cells exist up to higher Ro. A more quantitative study of the structures in rotating channel flow is presented in § 7.

At higher Ro the unstable turbulent side becomes smaller and smaller and the flow tends to fully laminarize if Ro approaches Ro_c (Wallin *et al.* 2013). Yet, even if $Ro \to Ro_c$, streamwise and oblique modes are still unstable as a result of rotation, according to linear stability theory (Brethouwer 2016), and some of the largest linearly unstable modes become noticeable in the DNS when turbulence becomes weak on the unstable channel side. Figure 4 shows the resulting typical oblique waves on the unstable side in a DNS at $Re = 30\,000$ and $Ro = 2.7$, close to $Ro_c = 2.87$ for this Re. The waves are quite weak, i.e. the wall-normal velocity is approximately 2 %–3 % of U_b in this case.

4. Flow statistics

In this section, one-point statistics of the flow are presented and the effects of rotation are discussed. As mentioned before, linearly unstable TS waves cause strong recurring bursts of turbulence on a long time scale in some DNS. The instabilities and bursts are the topic of another study (Brethouwer 2016), and therefore not

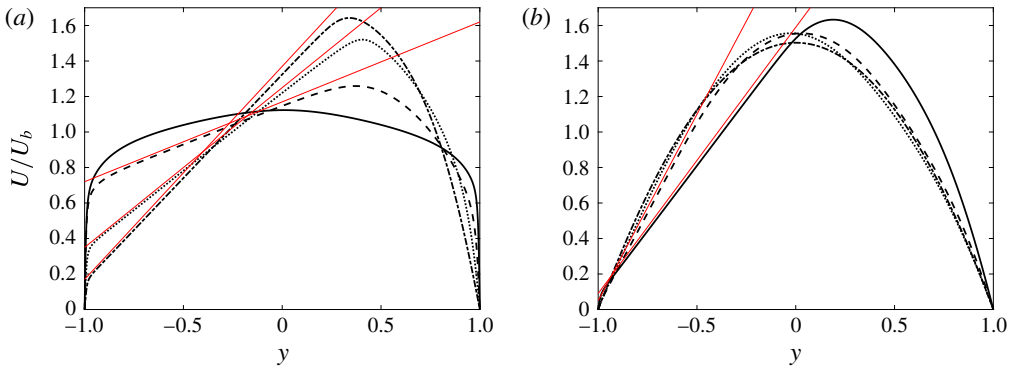

FIGURE 5. (Colour online) Mean velocity profiles scaled by U_b. (*a*) $Re = 31\,600$. ——, $Ro = 0$; – – –, $Ro = 0.45$; · · · · · ·, $Ro = 0.9$; – · – · –, $Ro = 1.2$. (*b*) $Re = 30\,000$. ——, $Ro = 1.5$; – – –, $Ro = 2.1$; · · · · · ·, $Ro = 2.4$; – · – · –, $Ro = 2.7$. Slopes with $S = -1$ are shown by straight red lines.

discussed in detail here. However, it should be noted that they significantly affect flow structures and turbulence, especially around the bursting moment and on the stable side where the bursts are most intense. Time series of, for instance, the volume-averaged turbulent kinetic energy K_m show distinct sharp peaks as a result of the bursts, while in the calm periods between the bursts the same quantity shows only small to moderate variations, see e.g. figure 3(*b*) in Brethouwer *et al.* (2014). I have excluded the burst periods when computing the statistics by excluding the periods with distinct peaks in K_m caused by the linear instability. The statistics are thus based on the long relatively calm periods of $O(100h/U_b)$ between the bursts when K_m only shows small to moderate variations and the turbulence does not appear to be strongly influenced by the instability. The reason for excluding these bursts periods from the statistics is that the bursts are not the subject of this study and that the bursts would obscure the direct effect of rotation on the turbulence. Besides, the bursts occur on a very long time scale of $O(1000h/U_b)$, which makes it practically impossible to obtain reasonable converged statistics if they are included, and they cannot be predicted by Reynolds stress and two-equation turbulence models. Brethouwer (2016) lists all the cases when bursts happen. At $Re = 30\,000$–$31\,600$, linear instabilities and bursts develop when $Ro \geqslant 1.2$. In the next parts, U is the mean streamwise velocity and u, v, w are the streamwise, wall-normal and spanwise velocity fluctuation, respectively. An overline implies temporal and spatial averaging in the homogeneous directions.

Figure 5 shows mean streamwise velocity profiles scaled by U_b at the highest Re considered for Ro up to 2.7. As in previous studies of turbulent channel flow subject to spanwise rotation (e.g. Kristoffersen & Andersson 1993; Grundestam *et al.* 2008; Xia *et al.* 2016), the mean velocity profile becomes asymmetric and develops an extended linear region where the slope $\mathrm{d}U/\mathrm{d}y \simeq 2\Omega$, i.e. $S \simeq -1$, implying an absolute mean vorticity close to zero. If $Ro \leqslant 1.5$ the velocity on the unstable side goes down, while on the stable side it goes up, since the turbulence becomes stronger and weaker on the unstable and stable side, respectively, as will be shown later. At higher Ro, the profile becomes more and more parabolic-like, and beyond $Ro = 2.4$ the linear slope region disappears and the velocity profile approaches a laminar Poiseuille profile, as in the DNS by Grundestam *et al.* (2008) and Xia *et al.* (2016).

Profiles of the root-mean-square (r.m.s.) of the streamwise, wall-normal and spanwise velocity fluctuations, u^+, v^+ and w^+, respectively, and the Reynolds shear

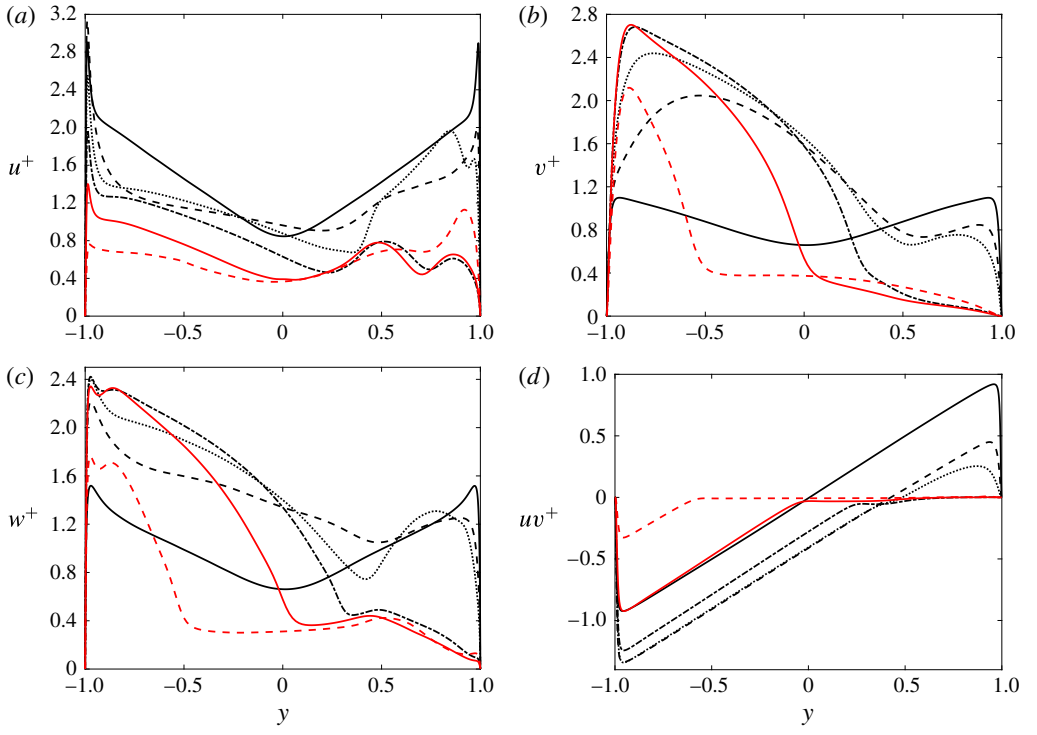

FIGURE 6. (Colour online) R.m.s. profiles of (*a*) streamwise, (*b*) wall-normal (*c*) spanwise velocity fluctuations and (*d*) $\overline{uv}$ profiles in wall units. $Re = 31\,600$ and (——) $Ro = 0$, (– – –) $Ro = 0.45$, (· · · · · ·) $Ro = 0.9$, (– · – · –) $Ro = 1.2$. $Re = 30\,000$ and (——, red) $Ro = 1.5$, (– – –, red) $Ro = 2.1$.

stress $\overline{uv}^+$ normalized by $u_\tau[u_{\tau u}^2/2 + u_{\tau s}^2/2]^{1/2}$ for Ro up to 2.1 are shown in figure 6. The results are for the highest Re considered here, 31 600 and 30 000. Note that for $Ro \geqslant 1.2$ the flow is subject to a TS wave instability, resulting in intense bursts of turbulence at this Re (Brethouwer 2016), but these periods with turbulent bursts are excluded as much as possible when computing the statistics, as mentioned before. The statistics are thus based on the long calm periods between the bursts.

Figure 6 shows that rotation causes a reduction of the turbulence intensity on the stable side, as expected (Johnston *et al.* 1972). Especially for the wall-normal component (figure 6*b*) this reduction is apparent, while for the other two velocity components it becomes most notable for $Ro \geqslant 1.2$. The turbulence on the unstable channel side displays a more complex behaviour. The peak of u^+ first rises with Ro but then declines if $Ro > 0.45$, whereas w^+, and especially v^+, grow strongly with Ro, and only start to notably decline when $Ro > 1.5$. At higher Ro, turbulence is progressively suppressed (not shown here) and the flow approaches more and more a laminar Poiseuille flow, as observed for the mean flow. Rotation thus has not only a marked influence on the turbulence intensity but also on its anisotropy, as in rotating homogeneous shear flows (Brethouwer 2005). The observed trends are in qualitative agreement with DNS of rotating channel flow at lower Re (Grundestam *et al.* 2008). The maximum of v^+ is near the wall at $Ro = 0$, but remarkably far from the wall on the unstable side at $Ro = 0.45$, which may be due to the presence of roll cells, while at higher Ro it approaches the wall again.

From the mean momentum balance for rotating channel flow follows

$$-\overline{uv} + \nu \frac{\mathrm{d}U}{\mathrm{d}y} = u_{\tau u}^2 - u_\tau^2 (y+1), \tag{4.1}$$

where the velocities are dimensional. The sum of the viscous and turbulent shear stresses is thus linear in y but is shifted owing to the difference in the wall shear stresses on the unstable and stable channel sides in the rotating flow cases. These stresses are naturally higher on the unstable side owing to the more intense turbulence. When viscous stresses are negligible the $\overline{uv}^+$ profile is also linear in y according to (4.1). From this equation it follows that in the part of the channel where $\nu\,\mathrm{d}U/\mathrm{d}y \simeq 2\nu\Omega = U_b^2 Ro/Re$ the turbulent shear stress is approximated as

$$\overline{uv} \simeq u_\tau^2 (y+1) - u_{\tau u}^2 + U_b^2 \frac{Ro}{Re}. \tag{4.2}$$

This shows that the $\overline{uv}^+$ profile is linear in y and has a unit slope even if viscous stresses are not negligible (Xia *et al.* 2016). Figure 6(*d*) confirms that on the unstable side the $\overline{uv}^+$ profiles have a unit slope. The turbulent momentum transfer shifts progressively towards the unstable side with Ro, and for $Ro \geqslant 1.2$ it is in fact negligible on the stable side where viscous stresses dominate. On the unstable side the magnitude of $\overline{uv}^+$ starts to decline when $Ro > 0.9$, and is small for $Ro \geqslant 2.1$. Viscous shear stresses are significant on the strongly turbulent unstable channel side at higher Ro because of the steep mean velocity gradient. If the total shear stress is estimated as u_τ^2, it follows that on the unstable side where $\mathrm{d}U/\mathrm{d}y \simeq 2\Omega$ the ratio between viscous and total stresses is approximately $Ro\,Re/Re_\tau^2$. From that it follows that the viscous contribution grows with Ro and is approximately 12 % and 26 % at $Re = 31\,600$ and $Ro = 1.2$ and 1.5, respectively, and even higher at the same Ro but lower Re. Once $Ro \gtrsim 2.0$, viscous stresses dominate also on the unstable side.

To investigate in more detail the turbulence near the wall on the unstable channel side, I present in figure 7 r.m.s.-profiles of the streamwise, wall-normal and spanwise velocity fluctuations, u^*, v^* and w^*, respectively, in viscous wall units of the unstable side using a logscale for y^*. Velocity fluctuations are thus scaled by $u_{\tau u}$ and $y^* = (y+1)u_{\tau u}/\nu$ since $u_{\tau u}$ appears to be the most relevant quantity very close to the wall. Note that $u_{\tau u}$ can deviate quite significantly from u_τ, see table 1. The peak of u^* on the unstable side declines and moves towards smaller y^* with Ro, whereas the peaks of v^* and w^* grow with Ro until $Ro = 1.5$ and then decline. This reduction and growth, respectively, are caused by an energy redistribution from streamwise to wall-normal fluctuations by the Coriolis term and pressure–strain correlations in the Reynolds stress equations, as will be shown later. The peak of w^* moves towards the wall with Ro, whereas that of v^* is found far away from the wall at $Ro = 0.45$ and comes closer to the wall with increasing Ro. The profile of w^* has two peaks for $Ro \geqslant 1.2$ which are accompanied by a double peak in the spectra, as shown later.

The skewness of the streamwise velocity $S(u)$ and wall-normal velocity fluctuations $S(v)$ are presented in figure 8. Profiles of $S(u)$ and $S(v)$ at lower Re are presented by Hsieh & Biringen (2016). $S(u)$ is typically negative away from the wall in non-rotating channel flow owing to ejections of low-speed fluid (Kim, Moin & Moser 1987). In rotating channel flow, $S(u)$ becomes considerably more negative near the wall at $Ro = 0.45$ and 0.9 on the unstable side, except very near the wall. This could be caused by a reduction of sweeping events of high-speed flow towards the wall as a consequence of rotation (Kristoffersen & Andersson 1993). On the other hand, the analysis by Dai

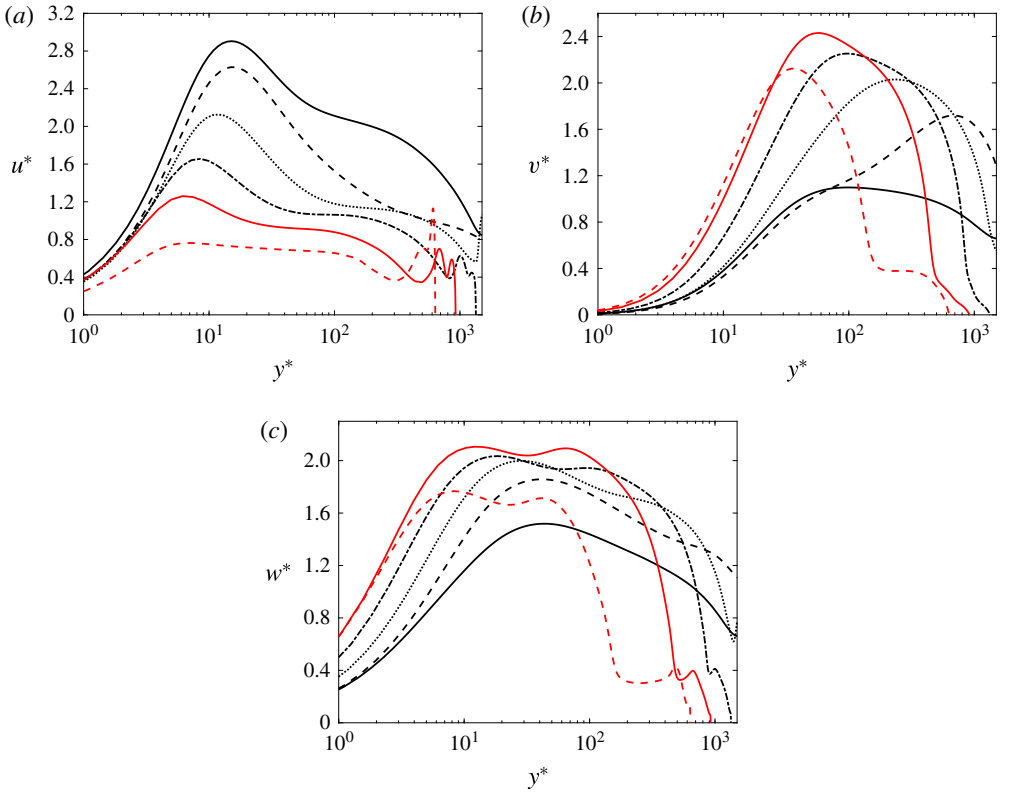

FIGURE 7. (Colour online) R.m.s. profiles of (*a*) streamwise, (*b*) wall-normal and (*c*) spanwise velocity fluctuations in wall units of the unstable side. $Re = 31\,600$ and (——) $Ro = 0$, (– – –) $Ro = 0.45$, (· · · · · ·) $Ro = 0.9$, (– · – · –) $Ro = 1.2$. $Re = 30\,000$ and (——, red) $Ro = 1.5$, (– – –, red) $Ro = 2.1$.

et al. (2016) indicates that under the influence of rotation the streaks become stronger on the unstable side, at least up to moderate Ro, which implies more or intenser ejections. The roll cells, observed before, could also play a role. If $Ro > 0.9$, $S(u)$ becomes less negative near the wall, which can be related to the weaker streaks and related ejections at high Ro, as suggested by Lamballais, Métais & Lesieur (1998). Further away from the wall, $S(u)$ attains small values in the rotating cases compared to the non-rotating case, indicating that sweeping and ejection events are significantly altered by rotation. $S(v)$ has a large positive value near the wall on the unstable side at $Ro = 0.45$ compared to $Ro = 0$, which is likely caused by roll cells that induce high-speed wall-normal velocity away from the wall. Similar behaviour of $S(v)$ was observed in the experiments by Nakabayashi & Kitoh (2005). Large positive values of $S(v)$, indicating events with large positive wall-normal velocities, are also found in all rotating cases on the unstable side, quite close to the position where the slope of U begins to deviate from 2Ω. At $Ro = 1.2$ and 1.5, $S(u)$ has large values at slightly larger y, near the position where U has its maximum value. The reason for the large values of $S(u)$ and $S(v)$ around these positions is not fully clear, but visualizations suggest that large values of v are found near the streamwise vortices visualized in figure 2. The large $S(u)$ could be related to the hairpin vortices seen in figure 2, since positive

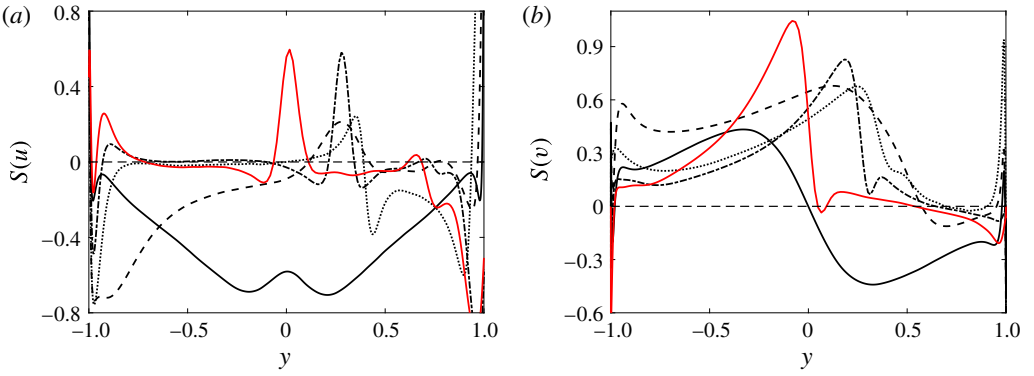

FIGURE 8. (Colour online) Skewness of (*a*) u and (*b*) v. $Re = 31\,600$ and (——) $Ro = 0$, (– – –) $Ro = 0.45$, (· · · · · ·) $Ro = 0.9$, (– · – · –) $Ro = 1.2$. $Re = 30\,000$ and (——, red) $Ro = 1.5$.

values of u are found above the head of such hairpin vortices (Christensen & Adrian 2001; Adrian 2007).

The flatness of the wall-normal velocity $F(v)$ attains extreme values in non-rotating channel flow very near the wall as a result of intense near-wall vortices (Lenaers *et al.* 2012). The present DNS show that, with faster rotation, $F(v)$ on the unstable channel side decays monotonically with Ro, suggesting that intense near-wall vortices are suppressed.

5. Influence of the Reynolds number

In this section, the influence of the Reynolds number on rotating channel flow at a fixed Ro is examined and shown to be significant. In a later section, this influence on the flow structures found on the unstable channel side is investigated.

Figure 9 shows profiles of the mean velocity U/U_b and fluctuations v^+ at $Ro = 0.15$, 0.45 and 0.9 for three to four Re. In all cases a region with a linear mean velocity profile where $S \simeq -1$ can be readily recognized, demonstrating once more that the appearance of a region with a zero absolute mean vorticity is a fundamental feature of rotating channel flow. Its extent and the closeness of $\mathrm{d}U/\mathrm{d}y$ to 2Ω do not show much variation with Re, and the same applies to the maximum value of v^+ on the unstable channel side. On the other hand, Re has an obvious influence on the mean velocity profile as well as v^+ on the stable channel side where, at higher Re, v^+ is considerably larger.

This Reynolds number effect is also observed in visualizations of the instantaneous streamwise velocity in a plane parallel and close to the wall on the stable channel side. At $Ro = 0.15$ and $Re = 20\,000$ the flow is fully turbulent on the stable channel side (figure 10*a*), whereas at a lower $Re = 3000$ the flow is largely laminar and contains only some turbulent spots (figure 10*b*), resulting in much lower turbulence levels on the stable channel side (figure 9*b*). At $Ro = 0.45$ and $Re = 31\,600$ a large fraction of the flow on the stable side is turbulent and turbulent–laminar patterns develop, as shown before in figure 1(*b*), whereas at the same Ro but lower $Re = 5000$ the flow is predominantly laminar and only one turbulent spot can be observed (figure 9*c*). At a lower $Re = 3000$ the spot is even smaller. Also at $Ro = 0.9$ and $Re = 31\,600$, regions with small-scale turbulence can be observed (figure 1*c*), but these regions with

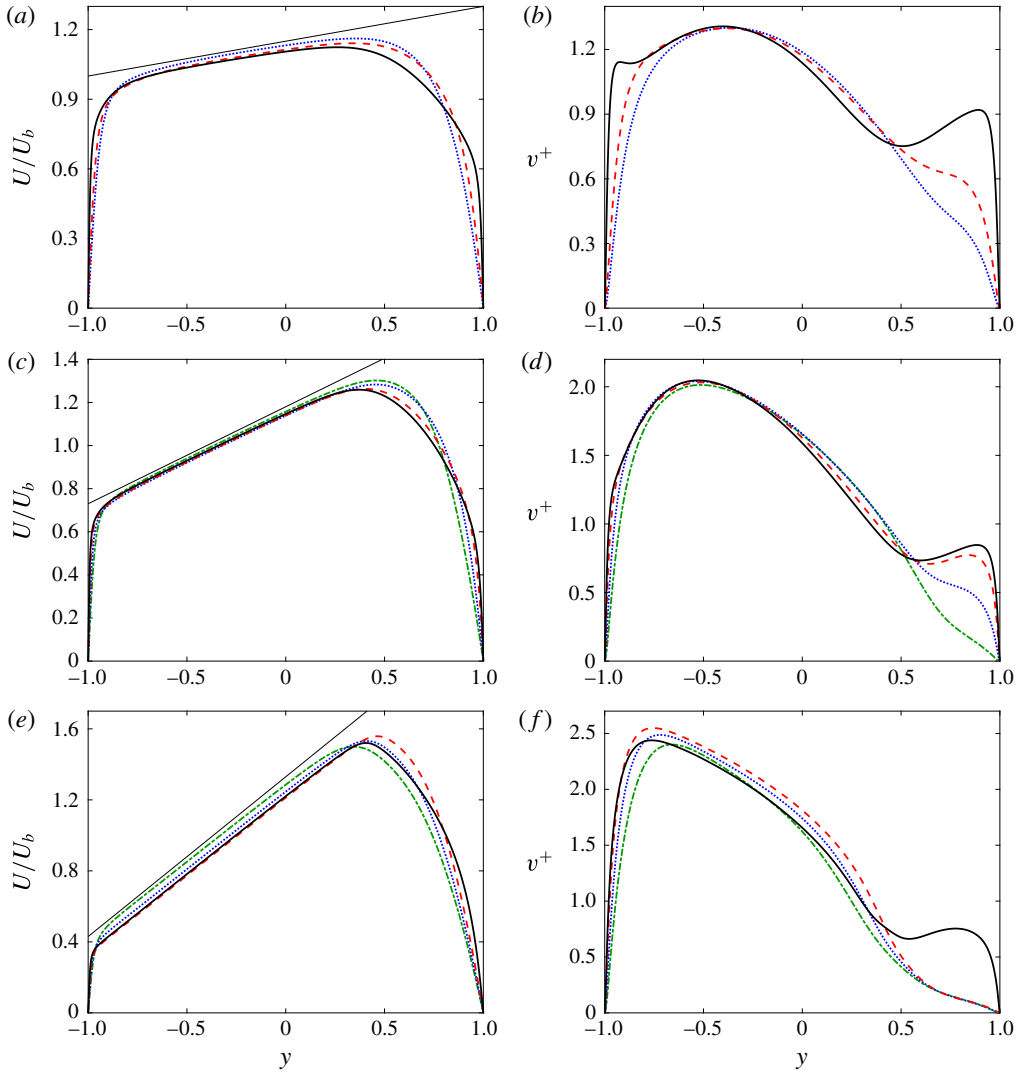

FIGURE 9. (Colour online) (*a*) Mean velocity profiles scaled by U_b and (*b*) r.m.s. of v in wall units at $Ro = 0.15$ and ——, $Re = 20\,000$; – – –, red, $Re = 5000$; · · · · · ·, blue, $Re = 3000$. (*c*) Mean velocity profiles scaled by U_b and (*d*) r.m.s. of v in wall units at $Ro = 0.45$ and ——, $Re = 31\,600$; – – –, red, $Re = 20\,000$; · · · · · ·, blue, $Re = 10\,000$; – · – · –, green, $Re = 5000$. (*e*) and (*f*) are the same as (*c*) and (*d*), respectively, but for $Ro = 0.9$. The straight black line has a slope $S = -1$.

small-scale turbulence are completely absent at lower Re (not shown here). Re thus has a marked influence on the flow, especially on the stable channel side, with a growing turbulent fraction and stronger turbulence at fixed Ro when Re gets higher. In the present study, oblique turbulent–laminar patterns have only been observed at higher Re. A speculation is that they also exist at low Re, although at a lower Ro when the stabilizing Coriolis force is less strong. But at a lower Re they can have a longer wavelength, as indicated by Brethouwer *et al.* (2012), implying that very large computational domains are required to resolve them.

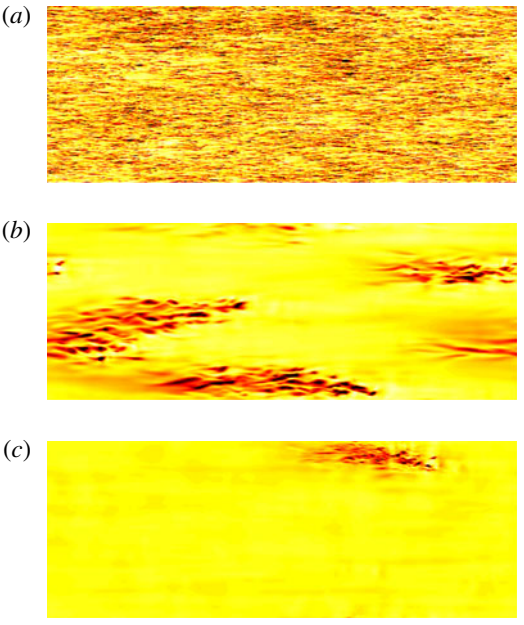

FIGURE 10. (Colour online) Visualizations of the instantaneous streamwise velocity in an x–z plane at $y^+ \approx 5$ on the stable channel side. Dark colours signify high velocities. (a) $Ro = 0.15$ and $Re = 20\,000$, (b) $Ro = 0.15$ and $Re = 3000$ and (c) $Ro = 0.45$ and $Re = 5000$.

Profiles of the r.m.s. of the velocity fluctuations in terms of wall units of the unstable side, i.e. velocity fluctuations scaled by $u_{\tau u}$ and $y^* = y u_{\tau u}/\nu$, for different Ro and Re are not presented here. However, the peak of the streamwise and spanwise fluctuations in general increases with Re at fixed Ro, whereas the maximum of the wall-normal fluctuations is quite independent of Re but moves towards larger y^* with Re.

The volume-averaged turbulent kinetic energy K_m scaled by U_b^2, mean wall shear stresses τ_w^u and τ_w^s on the unstable and stable channel sides, respectively, and skin friction coefficient $C_f = \tau_w/(\rho U_b^2/2)$ with $\tau_w = (\tau_w^u + \tau_w^s)/2$ are shown in figure 11 at different Ro and Re. Figure 11(a) shows that overall the turbulence intensity decays with Ro at fixed Re, and becomes very weak at high Ro, with similar trends for all Re. The data of Xia *et al.* (2016) are also included in the figure, and show first a 15 % growth in K_m/U_b^2 until $Ro = 0.44$, and then a quite similar decay as in the other cases; but note that in their DNS series $Re_\tau = 180$ and constant, and therefore Re varies. The difference in τ_w on the stable and unstable side first grows substantially with Ro until its maximum found at approximately $Ro = 0.9$, with the highest τ_w naturally occurring on the unstable side, but then diminishes and disappears at high Ro when the flow becomes laminar (figure 11b). Again, the trends are similar at different Re, but the maximum difference appears at lower Ro when Re is lower, and is smaller at the highest Re, possibly because the flow relaminarizes less fast on the stable side at higher Re, as discussed before. The skin friction C_f decays monotonically with Ro, like K_m, and nearly equals the value for laminar Poiseuille flow for $Ro \geqslant 2.4$ at all Re (figure 11c).

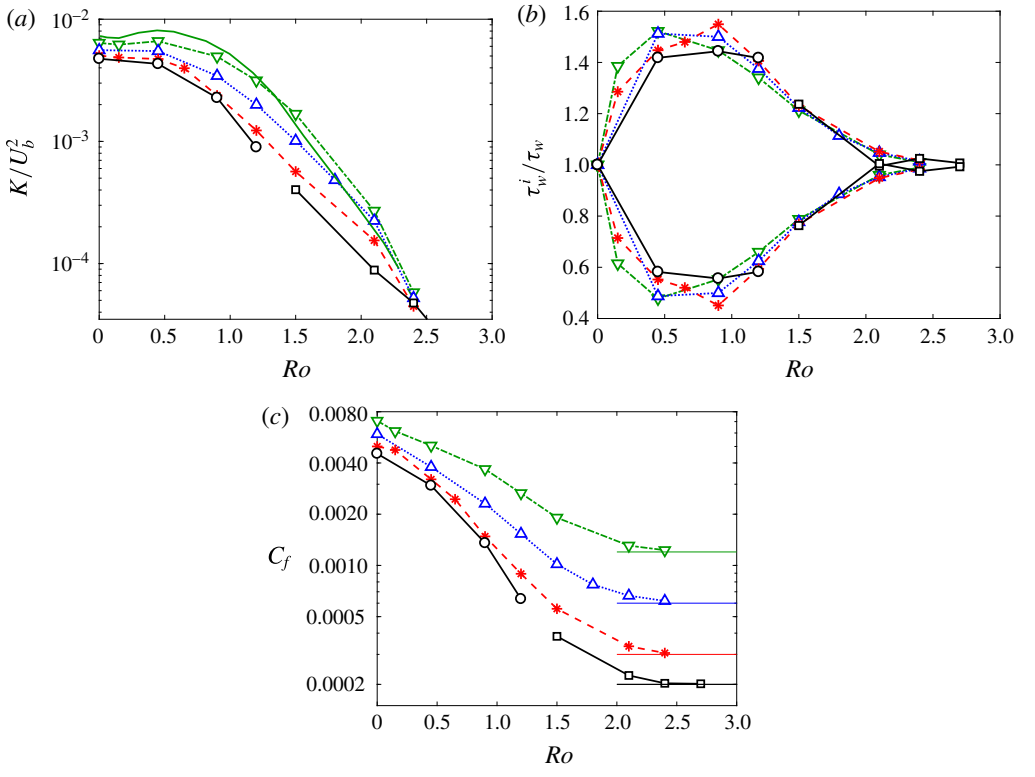

FIGURE 11. (Colour online) (*a*) $K_m/(U_b^2)$, (*b*) τ_w^u/τ_w (upper curves) and τ_w^s/τ_w, (*c*) C_f. ○—○, $Re = 31\,600$; □—□, $Re = 30\,000$; ∗−−−∗ (red), $Re = 20\,000$; Δ···Δ (blue), $Re = 10\,000$; ∇−·−·−∇ (green), $Re = 5000$; —— (green), $Re_\tau = 180$ (Xia *et al.* 2016). The horizontal line in (*c*) represents C_f for a laminar Poiseuille flow.

6. Balances

In this section, the balance terms in the transport equations of the turbulent kinetic energy and Reynolds stresses are studied. Grundestam *et al.* (2008) have also presented budgets for rotating channel flow, although only for one high $Ro = 1.5$ when the turbulence is very weak, while Xia *et al.* (2016) have only presented production terms. The present study contributes with a study of several budget terms at a significantly higher Re covering a wide Ro range.

From (4.2) it follows that the production of turbulent kinetic energy in the part of the channel, where $\mathrm{d}U/\mathrm{d}y \simeq 2\Omega$ is approximately (see also Xia *et al.* 2016)

$$P_K = -\overline{uv}\frac{\mathrm{d}U}{\mathrm{d}y} \simeq -2\overline{uv}\Omega = -\overline{uv}\frac{U_b}{h}Ro \simeq \left[u_{\tau u}^2 - u_\tau^2(y+1) - U_b^2\frac{Ro}{Re}\right]\frac{U_b}{h}Ro. \tag{6.1}$$

Consequently,

$$\frac{hP_K}{u_\tau^2 U_b Ro} \simeq -(y+1) + \left(\frac{u_{\tau u}}{u_\tau}\right)^2 - \left(\frac{U_b}{u_\tau}\right)^2\frac{Ro}{Re}. \tag{6.2}$$

Thus, the profile of P_K scaled with $u_\tau^2 U_b Ro/h = (u_\tau^4/\nu)(Ro_\tau/Re_\tau)$, where u_τ^4/ν is the usual viscous wall unit scaling, is expected to be approximately linear in y with a slope -1 in the part of the channel where $\mathrm{d}U/\mathrm{d}y \simeq 2\Omega$.

Figure 12(*a*) shows P_K scaled by $u_\tau^2 U_b Ro/h$ for Ro up to 2.1. The DNS results for $Ro = 0$ are included and scaled by $0.45u_\tau^2 U_b/h$, i.e. the same scaling as used for the $Ro = 0.45$ case. The profiles of P_K in the rotating cases show, as expected, a significant linear part with a -1 slope. In this part, the scaled P_K follows closely the prediction given by the right-hand side of (6.2). Similar linear profiles of P_K were observed in DNS of rotating channel flow at $Re_\tau = 180$ by Xia *et al.* (2016). Near the maximum of U, slight negative values of P_K are observed at some Ro, as in a DNS by Grundestam *et al.* (2008), which implies that some energy is transferred from turbulence to the mean flow in this region. The maximum value of P_K near the wall on the unstable side scales instead with viscous wall units since the peak of P_K lies between 0.244 and 0.248 for $Ro \leqslant 1.5$ when scaled by $u_{\tau u}^4/\nu$ (figure 12*b*).

In shear flows, the dissipation rate of turbulent kinetic energy, ε, is often approximately equal to the production of turbulent kinetic energy, P_K, which suggests that ε, like P_K, scales with $u_\tau^2 U_b Ro/h$. Figure 12(*c*) affirms that, in rotating channel flow, profiles of ε, scaled by $u_\tau^2 U_b Ro/h$, display a linear part. The DNS results for $Ro = 0$ are again included and scaled by $0.45u_\tau^2 U_b/h$. The slopes at $Ro = 0.45$ and $Ro = 2.1$ deviate from -1, but in the other three rotating cases they follow closely the prediction given by the right-hand side of (6.2). For $Ro \geqslant 0.9$, P_K and ε are in fact strikingly similar in the outer layer on the unstable channel side, much more so than at $Ro = 0$. The close balance between P_K and ε implies that the sum of turbulent, pressure and viscous diffusion in the equation for turbulent kinetic energy is small compared to P_K and ε. In terms of wall units, P_K and ε are large on the unstable side away from the wall in the rotating cases compared to the $Ro = 0$ case, whereas on the stable side both are very small if $Ro \geqslant 1.2$.

The observed scaling of P_K and ε with $u_\tau^2 U_b Ro/h$ suggests that this scaling is meaningful as well for the budget terms in the balance equation for the Reynolds stresses. This equation reads

$$\frac{\partial \overline{u_i u_j}}{\partial t} + U_k \frac{\partial \overline{u_i u_j}}{\partial x_k} = P_{ij} + \varepsilon_{ij} + C_{ij} + \Pi_{ij} + D_{ij}, \tag{6.3}$$

where the terms on the right-hand side are the production, dissipation, Coriolis, pressure–strain and diffusion term, respectively (Grundestam *et al.* 2008). The Coriolis terms in the equation for $\overline{uu}$, $\overline{vv}$, $\overline{ww}$ and $\overline{uv}$ stresses are $C_{uu} = 4\overline{uv}\Omega$, $C_{vv} = -4\overline{uv}\Omega$, $C_{ww} = 0$ and $C_{uv} = 2(\overline{vv} - \overline{uu})\Omega$, respectively. These terms do not perform work but transfer energy between the Reynolds stress components (Kawata & Alfredsson 2016). Note that $P_{uu} = 2P_K$.

Figure 12(*d*) shows the production of $\overline{uv}$ Reynolds stresses, $P_{uv} = -\overline{vv}\,\mathrm{d}U/\mathrm{d}y$, scaled by $u_\tau^2 U_b Ro/h$. Also in this figure and figure 13, data for $Ro = 0$ are included using the scaling $0.45u_\tau^2 U_b/h$ to make a comparison with data of rotating channel flow possible. The profiles of P_{uv} show less spreading than when using the ordinary wall unit scaling, and also reveal an approximately linear slope on the unstable side if $Ro \geqslant 0.9$. On the stable side, P_{uv} is significant at $Ro = 0.45$ but negligible for $Ro \geqslant 1.2$.

The Coriolis terms in the balance equations of the $\overline{uu}$ and $\overline{vv}$ Reynolds stresses are $C_{uu} = 2\overline{uv}/u_\tau^2$ and $C_{vv} = -2\overline{uv}/u_\tau^2 = -C_{uu}$, respectively, when scaled by $u_\tau^2 U_b Ro/h$. Profiles of $\overline{uv}/u_\tau^2$ were already presented in figure 6(*d*). From these profiles it follows that on the unstable side the Coriolis term transfers energy from $\overline{uu}$ to the $\overline{vv}$ component in rotating channel flow. On the stable side it is the other way around for $Ro = 0.45$ and 0.9, whereas it is small in the other cases.

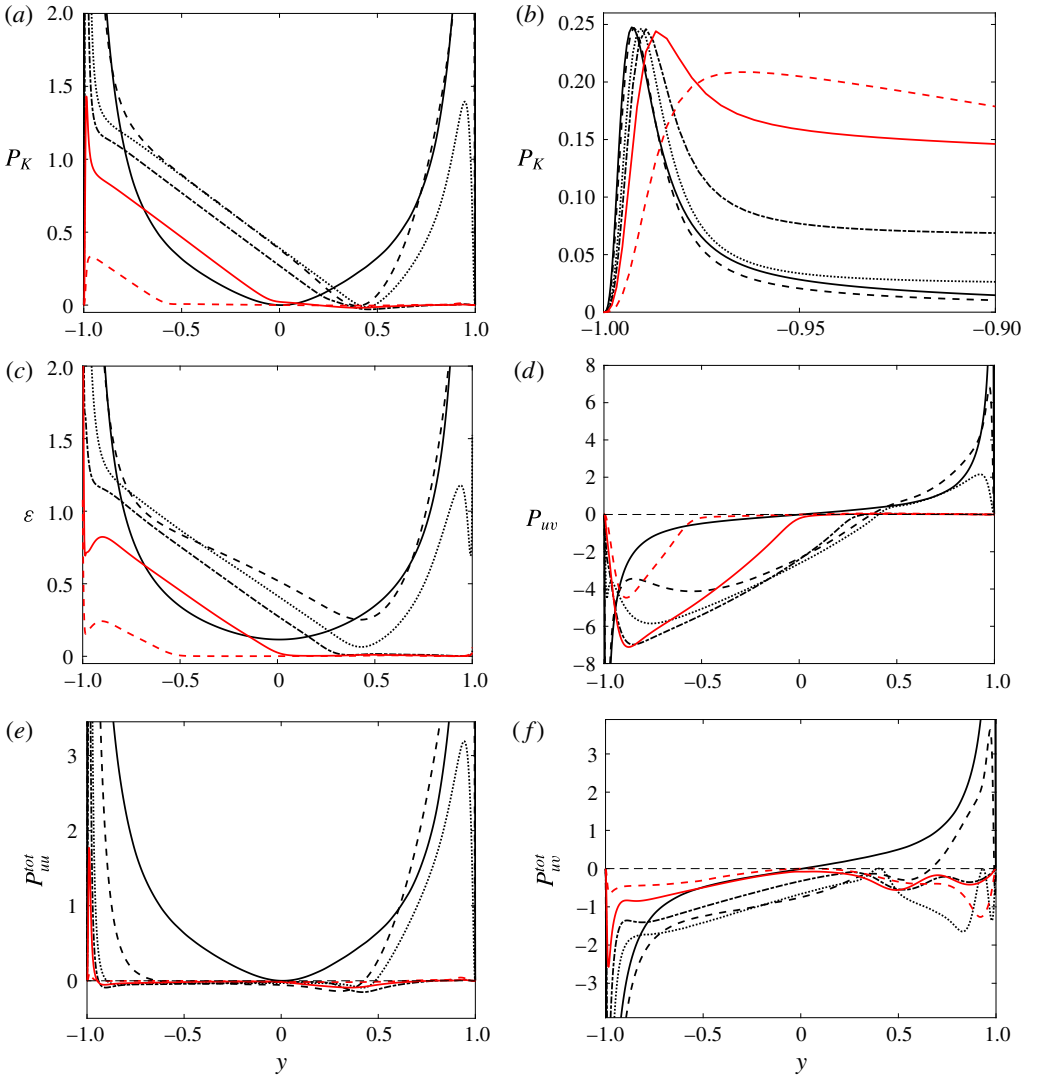

FIGURE 12. (Colour online) (*a*) P_K scaled by $u_\tau^2 U_b Ro/h$ and (*b*) P_K scaled by $u_{\tau u}^4/\nu$. (*c*) ε, (*d*) P_{uv}, (*e*) $P^{tot}_{uu} = P_{uu} + C_{uu}$ and (*f*) $P^{tot}_{uv} = P_{uv} + C_{uv}$, scaled by $u_\tau^2 U_b Ro/h$. $Re = 31\,600$ and (——) $Ro = 0$, (– – –) $Ro = 0.45$, (· · · · · ·) $Ro = 0.9$, (– · – · –) $Ro = 1.2$. $Re = 30\,000$ and (——, red) $Ro = 1.5$, (– – –, red) $Ro = 2.1$.

If $\mathrm{d}U/\mathrm{d}y \simeq 2\Omega$, $P_{uu} \simeq -4\overline{uv}\Omega = -C_{uu}$, which means that the Coriolis term closely balances the production term and, consequently, the dissipation term approximately balances the pressure–strain term in the equation for the $\overline{uu}$ component since the transport terms are small. This is confirmed by the DNS but not shown here. In fact, the sum $P_{ij} + C_{ij} \equiv P^{tot}_{ij}$ may be considered as a total production term. When $\mathrm{d}U/\mathrm{d}y \simeq 2\Omega$, $P^{tot}_{uu} \simeq 0$, $P^{tot}_{vv} \simeq P_{uu}$ and $P^{tot}_{ww} \simeq 0$, since $P_{uu} \simeq -C_{uu} = C_{vv}$ as explained above, and $P_{vv} = P_{ww} = C_{ww} = 0$. Figure 12(*e*) shows P^{tot}_{uu} scaled by $u_\tau^2 U_b Ro/h$ and confirms that in a large part of a rotating channel flow it is nearly zero. Thus, in a non-rotating flow, production feeds energy in the $\overline{uu}$ component and then energy is redistributed to the other components. By contrast, in rotating channel flow on

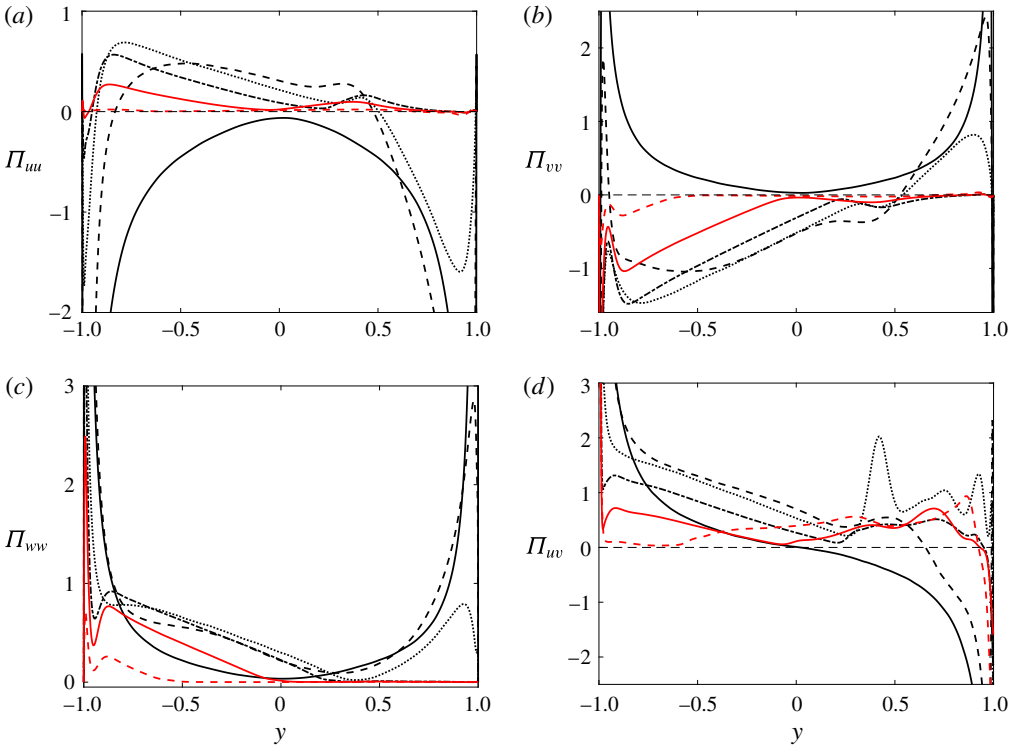

FIGURE 13. (Colour online) (*a*) Π_{uu}, (*b*) Π_{vv}, (*c*) Π_{ww} and (*d*) Π_{uv} scaled by $u_\tau^2 U_b Ro/h$. Lines used as in figure 12.

the unstable side, P_{ij}^{tot} feeds energy mainly in the $\overline{vv}$ component and pressure–strain correlations redistribute this energy to the $\overline{uu}$ and $\overline{ww}$ components. This may explain the strong wall-normal velocity fluctuations observed in rotating channel flow on the unstable side. Very near the wall on the unstable side, energy is still fed into the $\overline{uu}$ component. The same applies to the stable side for $Ro = 0.45$ and 0.9, but if $Ro \geqslant 1.2$ the sum is nearly zero. Note that P_{uu}^{tot} is slightly negative in rotating channel flow in a region around the maximum of U.

When scaled by $u_\tau^2 U_b Ro/h$, $C_{uv} = (\overline{vv} - \overline{uu})/u_\tau^2$. The total production P_{uv}^{tot} scaled by $u_\tau^2 U_b Ro/h$, shown in figure 12(*f*), is balanced by Π_{uv} since the dissipation and diffusion terms are relatively small in a large part of the channel, in particular on the unstable side. On the unstable side, P_{uv}^{tot} scaled is negative, but it becomes less negative for $Ro \geqslant 0.9$. On the stable side, it is positive at $Ro = 0.45$ and negative at larger Ro, meaning that it destroys $\overline{uv}$ correlations, leading to the low turbulent shear stresses on the stable side observed before.

Pressure–strain correlations Π_{uu}, Π_{vv}, Π_{ww} and Π_{uv} scaled by $u_\tau^2 U_b Ro/h$ are presented in figure 13. When $Ro = 0$, energy is transferred from $\overline{uu}$ to $\overline{vv}$ and $\overline{ww}$, whereas in the rotating cases energy is transferred from $\overline{vv}$ to $\overline{uu}$ and $\overline{ww}$ by pressure–strain correlations on the unstable side, except very close to the wall, where Π_{uu} is still negative. Especially at high Ro, Π_{ww} is large, which explains the strong spanwise fluctuations in rapidly rotating channel flows. On the stable side there is a significant energy transfer from $\overline{uu}$ to the other two components by pressure–strain correlations for $Ro \leqslant 0.9$. At larger Ro, Π_{uu} and Π_{vv} are small but not negligible on

the stable side, while Π_{uv} is positive (figure 13*d*) and approximately balanced by the Coriolis term C_{uv}, as discussed before. The slope of the pressure–strain profiles on the unstable side is also approximately linear for $Ro \geqslant 0.9$ and scales with $u_\tau^2 U_b Ro/h$.

Turbulent velocity fluctuations are not insignificant on the stable side (figure 6), although P_K is very small there for $Ro \geqslant 1.2$. Grundestam *et al.* (2008) have suggested that the turbulence on the stable side is forced by the turbulence on the unstable side through the pressure diffusion term of the $\overline{vv}$ component which then redistributes the energy through pressure–strain correlations. The pressure diffusion of $\overline{vv}$ indeed has a small positive value (not shown here) and figure 13(*a*,*b*) show that, albeit small, Π_{vv} is negative and Π_{uu} positive at $Ro = 1.2$ and 1.5 on the stable side. The latter is approximately balanced by a negative P_{uu}^{tot}.

7. Spectra and two-point correlations

In order to study the effect of rotation on turbulence structures in a quantitative way, Kristoffersen & Andersson (1993), Alvelius (1999) and Grundestam *et al.* (2008) computed two-point correlations at $Re_\tau = 180$–194. Kristoffersen and Andersson observed that the spanwise near-wall streak spacing in wall units narrows with Ro, whereas Alvelius observed the opposite trend. Generally, relatively short streamwise two-point correlations of streamwise fluctuations on the unstable side and relatively long correlations on the other laminar-like side were observed when the channel was rotating. At low Ro, Kristoffersen and Andersson and Alvelius were also able to notice an impact of Taylor–Görtler vortices on correlations on the unstable side.

Here, I present spanwise two-point correlations of the wall-normal velocity fluctuations as well as spectra, since they better reveal the impact of rotation on the different flow scales, especially the large scales which are known to become important at higher Re in wall flows (Smits, McKeon & Marusic 2011). Spectra of the streamwise velocity fluctuations are presented, since these most clearly reveal the presence of large-scale motions in non-rotating wall flows, as well as spectra of the spanwise and wall-normal velocity fluctuations, since these may uncover the presence of roll cells. The presented cospectra give information on the scales that contribute to the momentum transfer and production of turbulent kinetic energy. The focus is on the strongly turbulent unstable side of the channel. Spectra and two-point correlations are less instructive for the stable side when relaminarization occurs. First, I consider the trends with Ro and next with Re.

7.1. *Spectra at* $Re = 20\,000$

Spanwise premultiplied energy spectra, $k_z\Phi_{uu}$, $k_z\Phi_{vv}$ and $k_z\Phi_{ww}$ of the streamwise, wall-normal and spanwise velocity fluctuations, respectively, and cospectra, $k_z\Phi_{uv}$, at $Re = 20\,000$ are shown in figure 14. Streamwise premultiplied energy spectra, $k_x\Phi_{uu}$, $k_x\Phi_{vv}$ and $k_x\Phi_{ww}$ of the streamwise, wall-normal and spanwise velocity fluctuations, respectively, and cospectra, $k_x\Phi_{uv}$, at $Re = 20\,000$ are shown in figure 15. Spectra are shown for $Ro = 0$, 0.15, 0.45 and 0.9, and are presented as functions of the wall distance $y^* = (y+1)u_{\tau u}/\nu$ and the spanwise and streamwise wavelength λ_z^* and λ_x^*, respectively, both scaled in term of the viscous length scale of the unstable side, $l^* = \nu/u_{\tau u}$. The red dashed line in each plot indicates scales with a wavelength h. Spectra are scaled with their maximum values, which are given in terms of $u_{\tau u}$ in table 2.

Roll cells produce significant wall-normal and spanwise motions in rotating channel flow, as shown, for example, by Dai *et al.* (2016), and that can be expected to lead

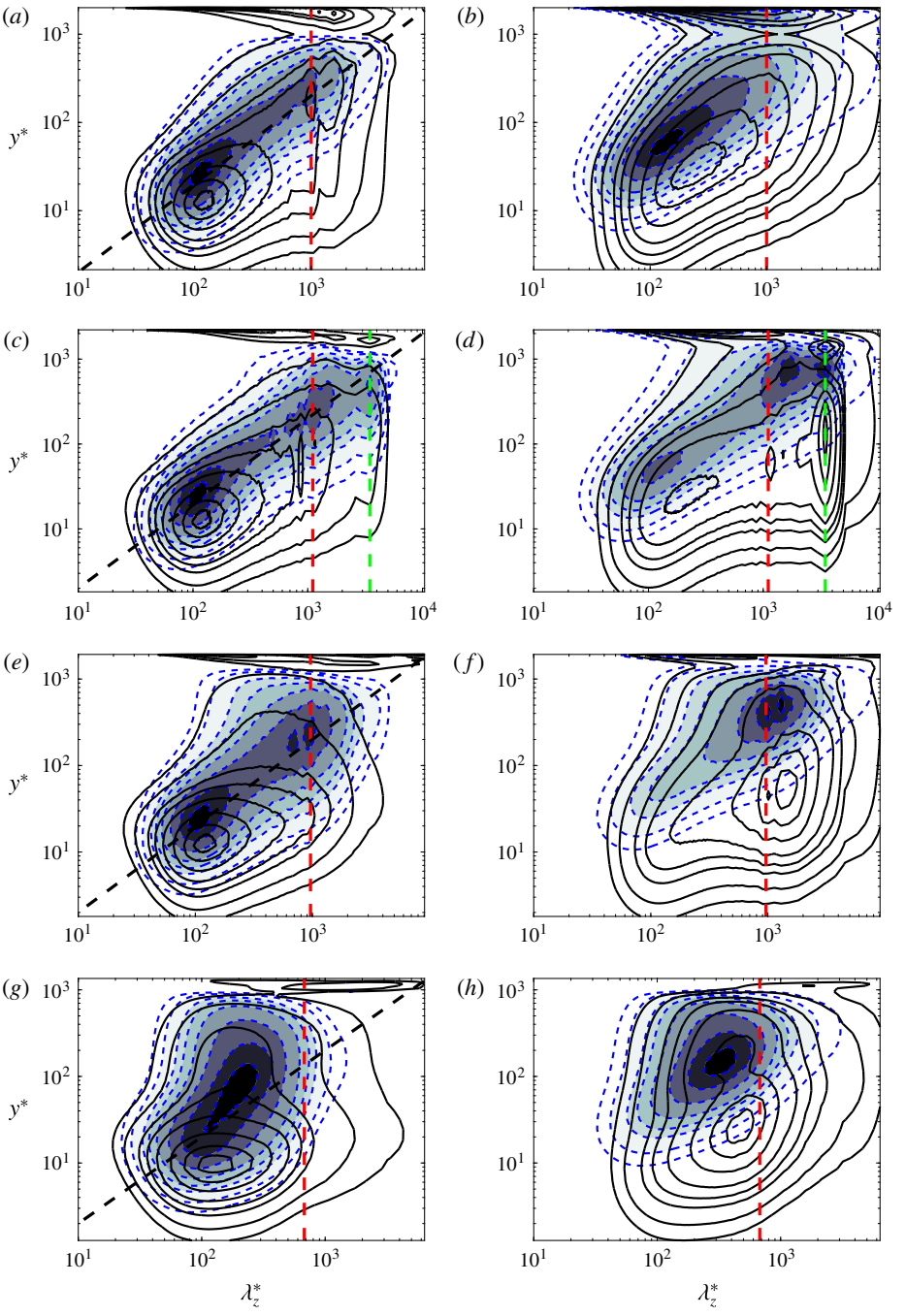

FIGURE 14. (Colour online) Maps of premultiplied one-dimensional energy spectra as function of spanwise wavelength λ_z^* and distance from the wall y^* at $Re = 20\,000$ for $Ro = 0$ (*a*,*b*), $Ro = 0.15$ (*c*,*d*), $Ro = 0.45$ (*e*,*f*) and $Ro = 0.9$ (*g*,*h*). (*a*,*c*,*e*,*g*) Shows $k_z\Phi_{uu}$ (black lines) and cospectra $k_z\Phi_{uv}$ (blue dashed lines and colours). (*b*,*d*,*f*,*h*) Shows $k_z\Phi_{vv}$ (blue dashed lines and colours) and $k_z\Phi_{ww}$ (black lines). Contour levels from innermost to outermost are 0.94, 0.8, 0.6, 0.4, 0.28, 0.2, 0.1 and 0.05. Spectra are scaled with their maximum value. The straight black dashed line follows the relation $y = 0.1\lambda_z$.

Re	Ro	$k_z\frac{\Phi_{uu}}{u_{\tau u}^2}^\star$	$k_z\frac{\Phi_{vv}}{u_{\tau u}^2}^\star$	$k_z\frac{\Phi_{ww}}{u_{\tau u}^2}^\star$	$k_z\frac{\Phi_{uv}}{u_{\tau u}^2}^\star$	$k_x\frac{\Phi_{uu}}{u_{\tau u}^2}^\star$	$k_x\frac{\Phi_{vv}}{u_{\tau u}^2}^\star$	$k_x\frac{\Phi_{ww}}{u_{\tau u}^2}^\star$	$k_x\frac{\Phi_{uv}}{u_{\tau u}^2}^\star$
20 000	0	3.83	0.56	0.73	0.58	2.13	0.40	0.66	0.28
20 000	0.15	3.85	0.75	1.00	0.57	2.15	0.32	0.56	0.28
20 000	0.45	3.01	1.60	1.39	0.49	1.89	0.59	0.64	0.27
20 000	0.9	1.67	2.13	1.86	0.46	1.24	1.04	0.95	0.29
5 000	0	—	0.50	0.64	—	—	0.33	0.57	—
5 000	0.45	—	1.61	1.32	—	—	0.61	0.61	—
5 000	0.9	—	2.50	1.85	—	—	1.16	0.96	—

TABLE 2. Maximum values of the premultiplied one-dimensional energy spectra. Superscript $\star$ means the maximum value of the quantity. The spectra are scaled with the friction velocity of the unstable side, $u_{\tau u}$.

to energetic large-scale modes in the spectra of the spanwise, and especially the wall-normal velocity, away from the wall. I therefore interpret distinctly energetic large-scale modes in the spanwise $k_z\Phi_{vv}$ and $k_z\Phi_{ww}$ spectra as well as in the streamwise $k_x\Phi_{vv}$ spectra as signs of roll cells. If there are n pairs of counter-rotating roll cells in the computational domain, which has a spanwise size of $L_z = 3\pi h$ in these DNS, the spanwise spectrum $k_z\Phi_{vv}$ can be expected to have a peak at $\lambda_z = 3\pi h/n$.

In non-rotating channel flow the spanwise spectra reveal, besides the streaks at $\lambda_z^* \approx 100$ indicated by the near-wall peak in $k_z\Phi_{uu}$, the signature of large wide structures of wavelength $\lambda_z \approx h$ in $k_z\Phi_{uu}$ and $k_z\Phi_{uv}$ further away from the wall (figure 14*a*), like in the DNS by Lee & Moser (2015). In the streamwise spectra $k_x\Phi_{uu}$ and $k_x\Phi_{uv}$, energetic peaks are seen at $\lambda_x^* \approx 1000$ near the wall, related to the near-wall cycle (Monty *et al.* 2009). In the outer layer, weakly energetic large-scale structures with wavelengths $\lambda_x \approx \pi h$ to $4\pi h$ are observed in $k_x\Phi_{uu}$ and $k_x\Phi_{uv}$ (figure 15*a*), which become more energetic at higher Re (Lee & Moser 2015).

The near-wall peak in the spanwise spectrum $k_z\Phi_{uu}$ and streamwise spectrum $k_x\Phi_{uu}$ changes little in the rotating cases if $Ro \leqslant 0.45$, so that a change of the streak spacing induced by rotation, as suggested by Kristoffersen & Andersson (1993) and Alvelius (1999), cannot be confirmed. However, at $Ro = 0.15$, $k_z\Phi_{vv}$ has three peaks caused by near-wall structures of wavelength $\lambda_z^* \approx 150$ around $y^* = 50$ and large structures with wavelengths $\lambda_z \approx \pi h/2$ and $\lambda_z \approx \pi h$ (the latter indicated by the green dashed line) in the outer layer of the unstable side far away from the wall at $y \approx -0.3$ (figure 14*d*). A strong large-scale peak is also observed in $k_z\Phi_{ww}$ at wavelength $\lambda_z \approx \pi h$ in the outer layer. The energetic large-scale modes in the outer layer at $\lambda_z \approx \pi h$ are almost certainly a consequence of three pairs of counter-rotating roll cells of spanwise size $\pi h/2$ seen previously in figure 3(*a*). The other peak in $k_z\Phi_{vv}$ at $\lambda_z = \pi h/2$ shows that there also smaller large-scale structures, possibly roll cells that are half the size of the largest ones, indicating that there might be roll cells of different sizes. Scales with the maximum possible streamwise wavelength, i.e. $\lambda_x = L_x$, are obviously energetic according to the streamwise spectra in figure 15(*c*,*d*), implying that at least some of the roll cells span the whole domain in the streamwise direction.

At a higher $Ro = 0.45$, the peaks in the spanwise spectra $k_z\Phi_{vv}$, $k_z\Phi_{ww}$ have, compared to the spectra at $Ro = 0$, clearly shifted towards larger scales (figure 14*f*), and those of the streamwise spectra $k_x\Phi_{vv}$, $k_x\Phi_{ww}$ to a streamwise wavelength $\lambda_x \approx 8\pi h/3$ (figure 15*f*) in the outer layer. The energetic large-scale modes observed in

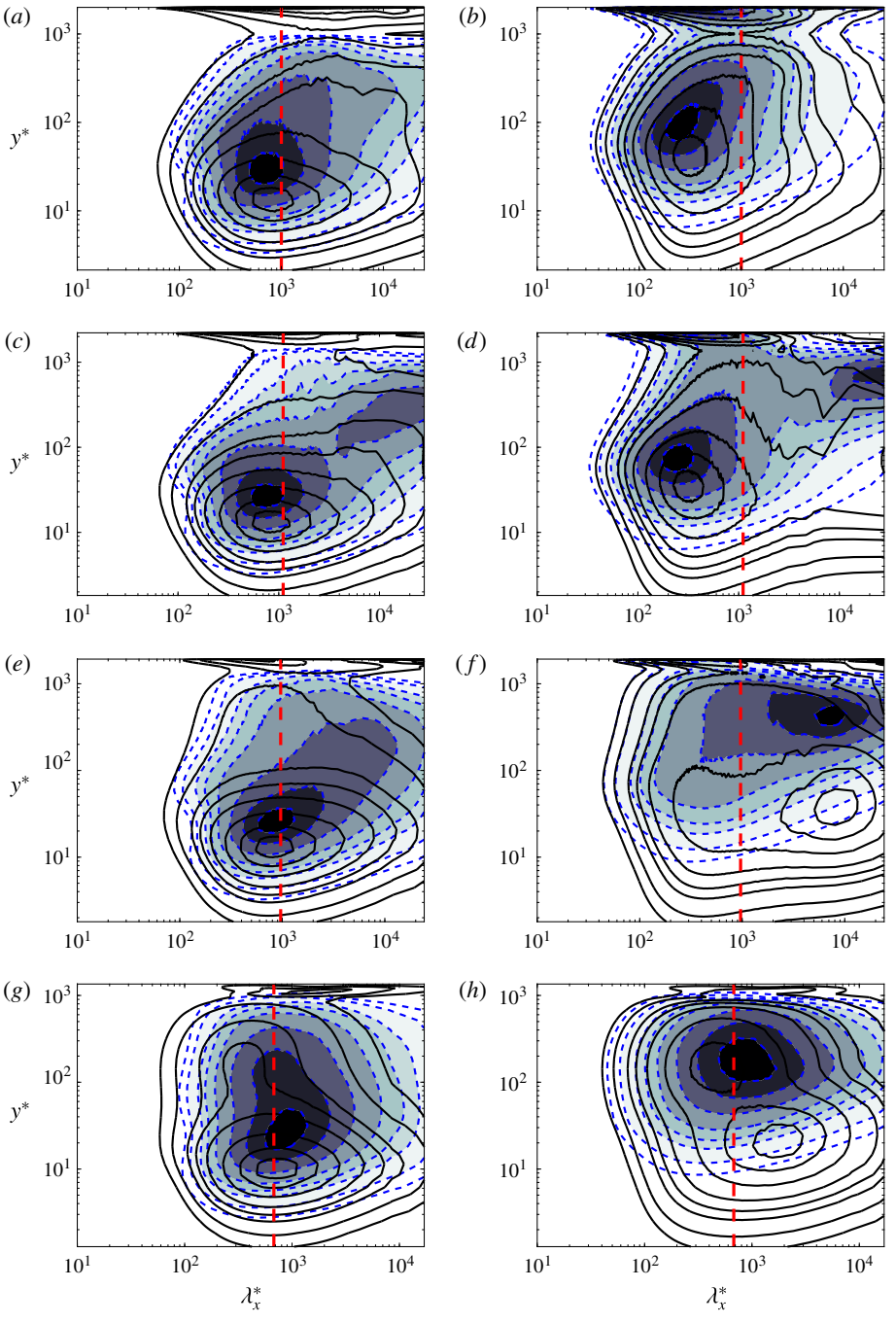

FIGURE 15. (Colour online) Maps of premultiplied one-dimensional energy spectra as function of streamwise wavelength λ_x^* and distance from the wall y^* at $Re = 20\,000$ for $Ro = 0$ (*a*,*b*), $Ro = 0.15$ (*c*,*d*), $Ro = 0.45$ (*e*,*f*) and $Ro = 0.9$ (*g*,*h*). (*a*,*c*,*e*,*g*) Shows $k_x\Phi_{uu}$ (black lines) and cospectra $k_x\Phi_{uv}$ (blue dashed lines and colours). (*b*,*d*,*f*,*h*) Shows $k_x\Phi_{vv}$ (blue dashed lines and colours) and $k_x\Phi_{ww}$ (black lines). Contour levels from innermost to outermost are 0.94, 0.8, 0.6, 0.4, 0.28, 0.2, 0.1 and 0.05. Spectra are scaled with their maximum value.

the spanwise spectrum $k_z\Phi_{vv}$ at $\lambda_z \approx 3\pi h/8$ and $y \approx -0.5$ are not present at $Ro = 0$; therefore, I interpret them as the signatures of roll cells. Two-point correlations, presented later, provide further evidence that they exist. The roll cells are smaller than at $Ro = 0.15$ and do not appear to span the whole streamwise domain according to the streamwise spectra, since the peak in the streamwise $k_x\Phi_{vv}$ is at $\lambda_x < L_x$. These observations are consistent with the results shown by the visualizations in figure 3 earlier. Dai *et al.* (2016) also noted that the roll cell diminished in size with Ro in their DNS at a much lower $Re = 2800$. In the present DNS, energetic wide and long structures in terms of outer units are observed as well in the spanwise and streamwise spectra Φ_{uu}, and especially the cospectra Φ_{uv} at $Ro = 0.45$, and even more so at $Ro = 0.15$ in the outer layer (figures 14*c*,*e* and 15*c*,*e*), showing that the roll cells induce large-scale momentum transfer.

Previous studies have found strong support for the hypothesis that the logarithmic region of wall-bounded turbulent flows is populated by attached eddies (Perry & Chong 1982) whose size grows with y, see e.g. Smits *et al.* (2011) and Hwang (2015). Some evidence of attached eddies can indeed be found in the present spanwise spectrum $k_z\Phi_{uu}$ and cospectrum $k_z\Phi_{uv}$ of the non-rotating channel flow (figure 14*a*), since they show that size of the structures grows with the distance to the wall in the logarithmic region. The cospectrum follows roughly the linear relation $y = 0.2\lambda_z - 1$ shown by the straight black dashed line in the figure, indicating that the size of eddies is approximately proportional to the distance to the wall, in agreement with the attached eddy hypothesis (Hwang 2015). The spanwise spectra $k_z\Phi_{uu}$ and cospectra $k_z\Phi_{uv}$ at $Ro = 0.15$ and 0.45 (figure 14*c*,*e*) show similar characteristics, with growing scales as y increases. The cospectrum also follows in these cases roughly the linear relation $y = 0.2\lambda_z - 1$. This provides support for the idea that rotating wall-bounded flows are also populated by attached eddies, at least up to moderate rotation rates.

At higher rotation rates, large-scale structures become progressively less energetic and smaller. At $Ro = 0.9$ no energetic large-scale structures are seen in the spanwise spectra $k_z\Phi_{uu}$ and $k_z\Phi_{uv}$, while $k_z\Phi_{vv}$ has a peak at spanwise wavelength $\lambda_z \approx \pi h/6$ in the outer layer at $y \approx -0.8$ (figure 14*g*,*h*). The streamwise spectrum of the streamwise velocity $k_x\Phi_{uu}$ has still a near-wall peak and that of the wall-normal velocity $k_x\Phi_{vv}$ has an outer peak at streamwise wavelength $\lambda_x \approx 2\pi h/5$, while the spectrum of the spanwise velocity $k_x\Phi_{ww}$ has two energetic peaks: an outer peak at streamwise wavelength $\lambda_x \approx \pi h/5$ and a near-wall peak at $\lambda_x \approx 4\pi h/5$ (figure 15*g*,*h*). Energetic large-scale roll cells are thus not present according to the spectra – correspondingly, no large structures like roll cells are observed in visualizations, and there are fewer energetic large-scale motions that contribute to momentum transfer than in a non-rotating channel flow.

Similar observations (not shown for brevity) are made at yet higher Ro, i.e. no energetic wide or long structures are present according to the spectra and cospectra in terms of outer units. The peak in the spanwise spectrum $k_z\Phi_{vv}$ shifts towards shorter wavelengths and the double peak in the streamwise spectrum $k_x\Phi_{ww}$ persists. The double peak is also observed in the r.m.s. profiles (figure 6*c*). The spanwise spectra $k_z\Phi_{uu}$ and $k_z\Phi_{uv}$ still have a spectral peak at $\lambda_z^* \approx 100$, but the peak moves closer to the wall in terms of viscous wall units. The streamwise spectra $k_x\Phi_{uu}$ and $k_x\Phi_{uv}$ have a spectral peak at $\lambda_x \approx h$ when $Ro \geqslant 0.9$, but in terms of the viscous wall units the structures become shorter. This means that the near-wall streaky structures move closer to the wall and become shorter, in agreement with the results of Lamballais *et al.* (1998), but they do not clearly confirm their finding that these structures become weaker at high Ro.

According to the spanwise spectrum $k_z\Phi_{uu}$ and cospectrum $k_z\Phi_{uv}$ at $Ro = 0.9$ (figure 14*g*), the structures do not become much larger when the distance to the wall increases, and at higher Ro the scales appear to grow even less with y. The absence of structures whose size grows with the distance to the walls when $Ro \gtrsim 0.9$ implies that attached eddies are much less prominent in very rapidly rotating wall-bounded flows. This suggests that the interaction between the inner and outer layer is weak at high Ro. Pressure and turbulent diffusion of turbulent kinetic energy are accordingly very small on the unstable side in that case.

Spectra at $Re = 20\,000$ and $Ro = 0.15$ at the stable side of the channel (not shown here) show that the roll cells observed on the unstable side do not deeply penetrate the stable channel side, although the study by Dai *et al.* (2016) shows that they occasionally can become larger and may even affect the flow up to the wall at the stable channel side. The spectra also show energetic near-wall modes at $\lambda_z^* \approx 100$ and $\lambda_x^* \approx 800$, as on the unstable side, implying that the near-wall cycle is maintained. On the other hand, although the flow is fully turbulent on the stable side at this low Ro, the spectra on the stable channel side reveal no or much less energetic large-scale modes than at $Ro = 0$, showing that cyclonic rotation weakens large-scale structures in wall-bounded flows. This agrees with the observation that in plane Couette flow even very weak cyclonic spanwise rotation eliminates large-scale structures (Komminaho, Lundbladh & Johansson 1996).

7.2. *Reynolds number dependence*

In several other DNS studies of spanwise rotating channel flow, large streamwise roll cells or Taylor–Görtler vortices have been found and examined, as mentioned before. Kristoffersen & Andersson (1993), Lamballais *et al.* (1998), Dai *et al.* (2016) and Hsieh & Biringen (2016) have observed them in DNS at $Re_\tau \leqslant 200$ and $Ro \leqslant 0.5$. Hsieh and Biringen have observed them also at $Re_\tau = 406$ and $Ro = 0.2$. It is important that the roll cells are properly resolved since flow statistics deviate significantly if they are suppressed (Hsieh & Biringen 2016). Helical spectra computed from DNS at $Re_\tau = 180$ by Yang & Wu (2012) suggest large roll cells if $0.03 \leqslant Ro \leqslant 0.57$, with the strongest signal at $Ro = 0.15$. The size of the roll cells appears to diminish with Ro for $Ro \geqslant 0.15$, and there is no sign that they exist at $Ro = 0.94$ and higher. On the other hand, visualizations and spanwise two-point correlations computed by Grundestam *et al.* (2008) at $Re_\tau = 180$ indicate that roll cells are present at $Ro = 1.27$, but the statistics show that the roll cells are non-stationary and do not have a long correlation length in the streamwise direction, and their size appears to be smaller than at lower Ro.

Thus, there is strong evidence that large roll cells exist in spanwise rotating channel flow at low Reynolds numbers for $Ro \lesssim 0.6$. At higher Ro, roll cells are less certain and more difficult to detect owing to their unsteadiness, but there are indications of their occurrence (Grundestam *et al.* 2008). Spectra presented before reveal large streamwise roll cells in a DNS at $Re = 20\,000$ and $Ro = 0.15$, and clearly hint at their occurrence at $Ro = 0.45$, but at $Ro = 0.9$ and higher there is no strong evidence of their presence. This suggests that, at lower Reynolds numbers, roll cells exist in a wider Ro range. Note, that in previous DNS of rotating channel flow the computational domain size was $4\pi \times 2\pi$ in the streamwise and spanwise directions, respectively, or less, which is smaller than in the present DNS. This may influence the size and enhance the coherency of the roll cells, especially in combination with periodic boundary conditions. Indeed, in the DNS by Kristoffersen & Andersson

(1993) at $Ro = 0.15$ the roll cells were very steady, whereas in the experiments by Johnston *et al.* (1972) the boundary conditions were different and the roll cells were much more unsteady.

To answer more unequivocally whether at low Re roll cells exist in a wider Ro range than at higher Re, I have computed premultiplied one-dimensional spanwise and streamwise spectra of the wall-normal and spanwise velocity fluctuations at $Re = 5000$ for $Ro = 0$, 0.15, 0.45 and 0.9, see figure 16. The wavelength and the distance to the wall is, as in the previous spectra, scaled by the viscous length scale of the unstable side, $l^* = \nu/u_{\tau u}$, and the spectra are scaled with their maximum value, see table 2. The red dashed line marks again scales with a wavelength h. Spanwise two-point correlations of the wall-normal velocity fluctuations $R_{vv} = \overline{v(\boldsymbol{x}+z)v(\boldsymbol{x})}/\overline{vv}$ at $Re = 3000$, 5000 and 20 000 and various Ro have also been calculated. If streamwise vortices are present, R_{vv} is expected to display negative correlations with a minimum at a separation distance that is approximately equal to the mean vortex diameter. Accordingly, in non-rotating channel flow, R_{vv} has a minimum at $z^* \approx 25$ near the wall as a result of near-wall streamwise vortices (Kim *et al.* 1987). The two-point correlations are shown at the unstable channel side at the wall-normal position, where R_{vv} approximately has the largest negative values and thus the signs of the roll cells are most clear. In all cases, the mean velocity profile is approximately linear at this position. The domain size is the same in all DNS used to compute the spectra and two-point correlations.

At $Ro = 0.15$ and $Re = 5000$, the spanwise spectrum $k_z\Phi_{ww}$ has a peak at $\lambda_z = \pi h$ (indicated by the green dashed line) while the peak of $k_z\Phi_{vv}$ extends from approximately $\lambda_z = \pi h/2$ to πh (figure 16*c*) and the streamwise spectra reveal structures that span the whole streamwise domain (figure 16*d*). Spectra at $Re = 3000$ are not shown for brevity, but at $Ro = 0.15$ they show a peak at spanwise wavelengths $\lambda_z = \pi h$ and a lesser one at $3\pi h/5$. This indicates, similarly as at $Re = 20\,000$, roll cells with a size of $\pi h/2$ and smaller ones. By comparing figure 16(*e*,*f*) with figure 16(*a*,*b*), it can be concluded that, at $Ro = 0.45$, wider and longer structures exist on the unstable channel side than at $Ro = 0$, implying that large roll cells are present. The spectral peaks in the spanwise $k_z\Phi_{vv}$ and streamwise spectrum $k_x\Phi_{vv}$ are at $\lambda_z \approx 3\pi h/8$ and $\lambda_x \approx 2\pi h$, respectively. At similar wavelengths, peaks are found in the spectra at $Re = 20\,000$, as shown before, and $Re = 3000$.

The spectra suggest that the roll cells at $Ro = 0.15$ as well as at $Ro = 0.45$ have a similar size for $Re = 3000$–$20\,000$. This is confirmed by the two-point correlations. At $Ro = 0.15$, R_{vv} is clearly negative for $0.5 \lesssim z \lesssim 2$, and its minimum, which is a measure of the mean vortex diameter, is at approximately the same z at all three Reynolds numbers (figure 17*a*). The spectra suggest roll cells with a diameter $\pi h/2$ as well as smaller ones, and that appears to be consistent with the two-point correlations which suggest roll cells with a mean diameter of approximately h. Also R_{vv} at $Ro = 0.45$ has a minimum at approximately the same z at all three Re (figure 17*b*). The spectra indicate that the roll cells have a mean diameter of approximately $3\pi h/16$, in agreement with the two-point correlations.

These results indicate that for $Re = 3000$–$20\,000$ the size of the roll cells is smaller at $Ro = 0.45$ than at $Ro = 0.15$, but approximately independent of Re. The size $\pi h/2$ of the largest roll cells at $Ro = 0.15$ indicated by the spanwise spectra is consistent with the size observed in the DNS by Kristoffersen & Andersson (1993) and Yang & Wu (2012) at the same Ro. Yang and Wu also observed smaller roll cells and found that the size of the roll cells becomes smaller with Ro for $Ro \geqslant 0.15$, again consistent with the present results. Also the DNS by Dai *et al.* (2016) at $Re = 2800$ show that the roll

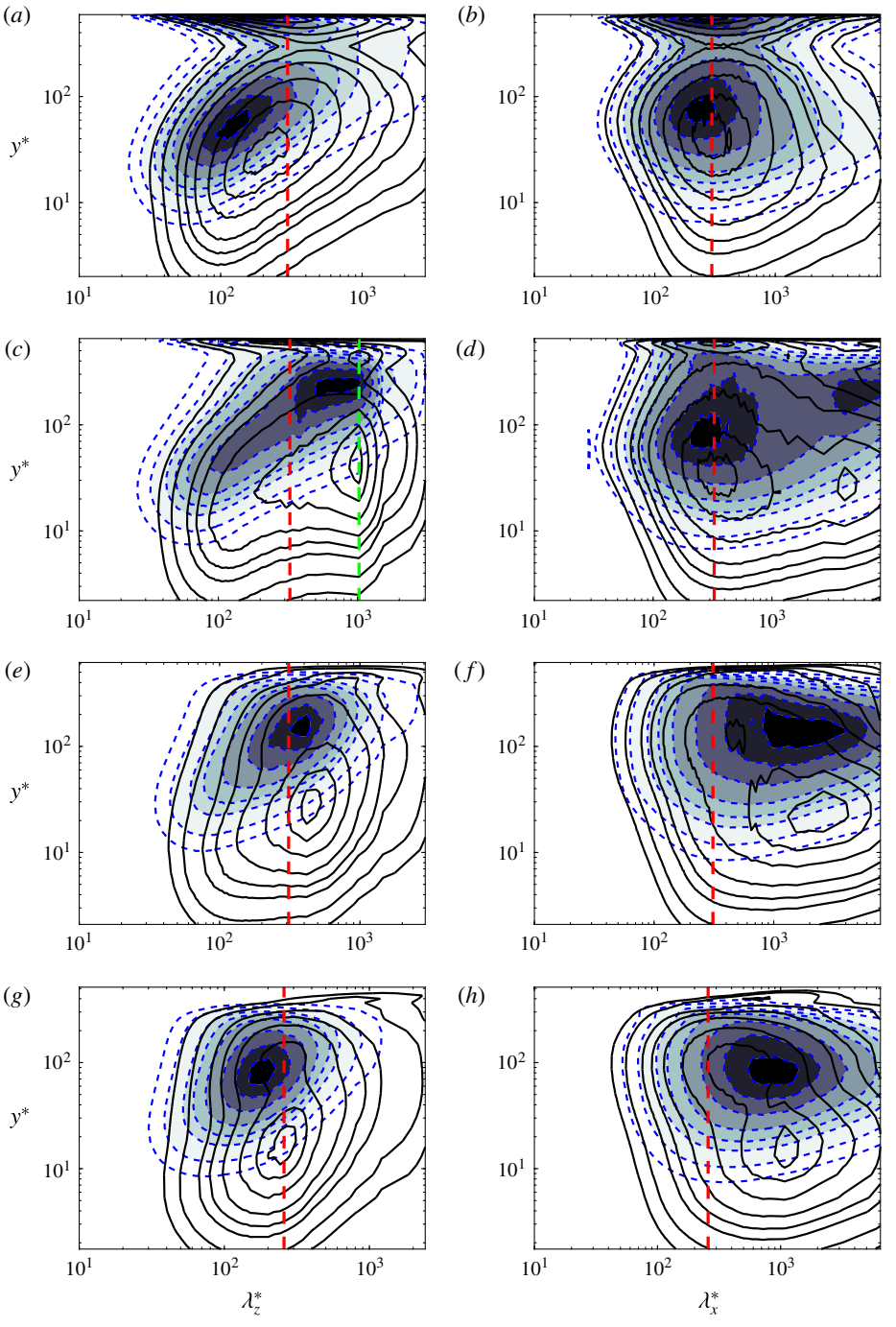

FIGURE 16. (Colour online) Maps of premultiplied one-dimensional spanwise and streamwise energy spectra at $Re = 5000$ for $Ro = 0$ (*a*,*b*), $Ro = 0.15$ (*c*,*d*), $Ro = 0.45$ (*e*,*f*) and $Ro = 0.9$ (*g*,*h*). (*a*,*c*,*e*,*g*) Shows spanwise spectra $k_z\Phi_{vv}$ (blue dashed lines and colours) and $k_z\Phi_{ww}$ (black lines). (*b*,*d*,*f*,*h*) Shows streamwise spectra $k_x\Phi_{vv}$ (blue dashed lines and colours) and $k_x\Phi_{ww}$ (black lines). Contour levels from innermost to outermost are 0.94, 0.8, 0.6, 0.4, 0.28, 0.2, 0.1 and 0.05. Spectra are scaled with their maximum value.

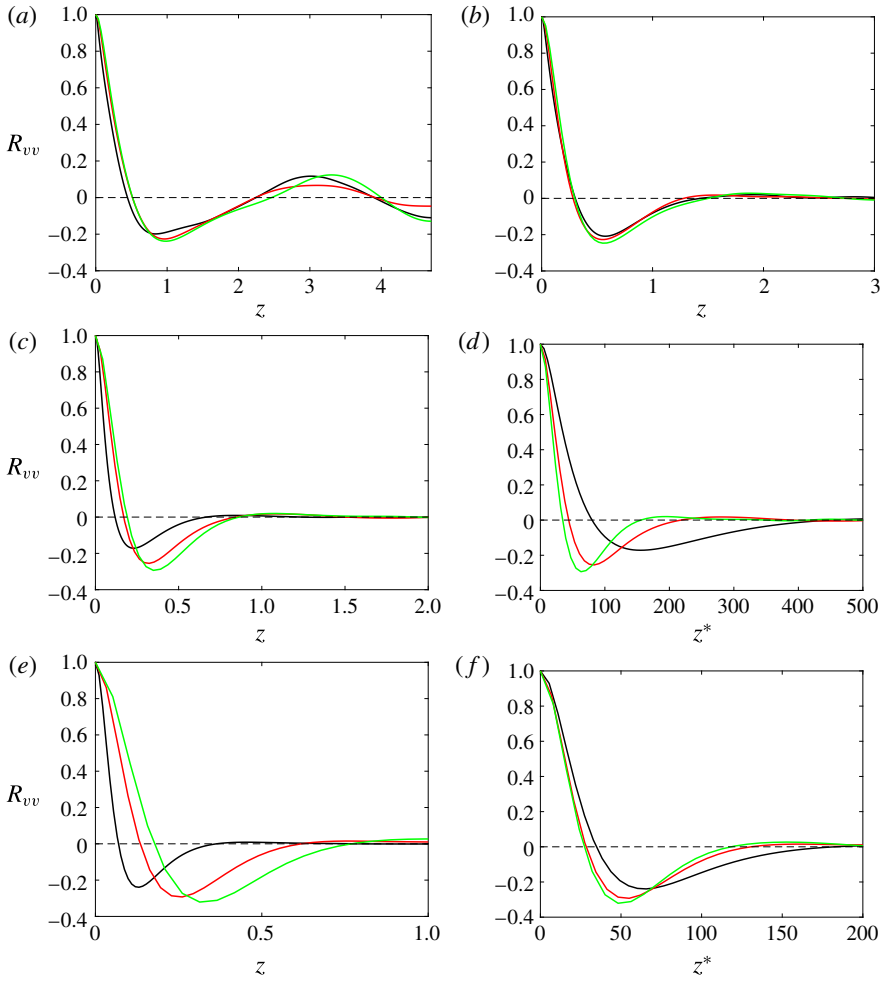

FIGURE 17. (Colour online) Spanwise two-point correlations of the wall-normal velocity fluctuations at (*a*) $Ro = 0.15$ and $Re = 20\,000$ and $y = -0.41$, $Re = 5000$ and $y = 0$, and $Re = 3000$ and $y = 0$; (*b*) $Ro = 0.45$ and $Re = 20\,000$ and $y = -0.54$, $Re = 5000$ and $y = -0.55$, and $Re = 3000$ and $y = -0.5$; (*c*,*d*) $Ro = 0.9$ and $Re = 20\,000$ and $y = -0.83$, $Re = 5000$ and $y = -0.75$, and $Re = 3000$ and $y = -0.75$; (*e*,*f*) $Ro = 1.2$ and $Re = 20\,000$ and $y = -0.92$, $Re = 5000$ and $y = -0.83$, and $Re = 3000$ and $y = -0.75$. In (*a*,*b*,*c*,*e*) z is scaled by h and in (*d*,*f*) $z^* = z/l^*$. (——, black) $Re = 20\,000$, (——, red) $Re = 5000$ and (——, green) $Re = 3000$.

cells become smaller when Ro increases from 0.1 to 0.5. On the other hand, the size $\pi h/2$ of the roll cells in the DNS by Hsieh & Biringen (2016) at $Ro = 0.5$ and $Re_\tau \approx 200$ is considerably larger than in the present DNS at $Ro = 0.45$. This difference might be related to the more restricted computational domain used by Hsieh and Biringen. Besides, they only show visualizations of the time-averaged velocity field, and these naturally emphasize the largest, most steady structures.

At a higher $Ro = 0.9$, the peak in the spanwise spectrum $k_z\Phi_{vv}$ shifts towards a smaller $\lambda_z \approx 3\pi h/13$ at $Re = 5000$ (figure 16*g*) and $\lambda_z \approx 3\pi h/11$ at $Re = 3000$, which is at a larger wavelength than at $Re = 20\,000$ (figure 14*h*). The large structures are

also considerably longer in terms of outer units at lower Re, see figure 16(h) versus figure 15(h). The minimum in R_{vv} shifts towards smaller z at higher Re (figure 17c), confirming that at $Ro = 0.9$ the large scales become smaller at higher Re. The two-point correlations (figure 17e) and spectra (not shown here) show that at $Ro = 1.2$ the differences are even more pronounced. The size of the large flow structures in terms of outer units shrinks monotonically with Re, and this trend continues at higher Ro. On the other hand, if the separation distance z is scaled by the viscous length scale l^*, the two-point correlations differ considerably at $Ro = 0.9$ (figure 17d) and lower Ro, but much less at $Ro = 1.2$ (figure 17f) and higher Ro. The two-point correlations at $Re = 3000$ and $Re = 5000$ show in fact an almost perfect collapse. Thus, the size of the largest scales continues to decrease with Ro, but for $Ro \geqslant 0.9$ it becomes dependent on Re as well. Whether these largest structures can be considered to be typical roll cells is not clear since the roll cells and typical near-wall streamwise vortices become less distinguishable at high Ro and low Re. The two-point correlations suggest that their size starts to display a viscous wall unit scaling and therefore may not have the same physical origin as at lower Ro.

8. Conclusions

The present numerical study of fully developed plane turbulent channel flow subject to system rotation about the spanwise direction covers a wide range of parameters with Re between 3000 and 31 600 and Ro between 0 and 2.7. At all Re, and for a wide range of Ro, the mean streamwise velocity profile has a linear part with a slope $\mathrm{d}U/\mathrm{d}y \simeq 2\Omega$, implying that this mean zero-absolute-vorticity state is independent of the Reynolds number. This zero-absolute-vorticity state has also been found in low Reynolds number and approximately in transitional rotating channel flow (Iida *et al.* 2010; Wall & Nagata 2013) and in laminar and turbulent plane Couette flow subject to anticyclonic rotation (Gai *et al.* 2016; Kawata & Alfredsson 2016). In all these other cases, the flow is dominated by large streamwise roll cells. Hsieh & Biringen (2016) found that when roll cells are suppressed in DNS of rotating turbulent channel flow by decreasing the spanwise domain size, the slope of the mean velocity profile $\mathrm{d}U/\mathrm{d}y$ deviates from 2Ω, pointing out that it is important to resolve the roll cells. In the present study, the zero-absolute-vorticity state also exists at high Ro when the flow is turbulent but roll cells are absent or small, proving that roll cells are not a prerequisite. Some possible explanations for the zero-absolute-vorticity state have been proposed (Hamba 2006; Kawata & Alfredsson 2016), but none rigorous. Because of the linear mean velocity slope, profiles of the production and dissipation rate of turbulent kinetic energy and some of the budget terms in the Reynolds stress equations show a linear part as well. In this part of the unstable channel side, basically all energy is fed into the wall-normal Reynolds stress component when the production and Coriolis term are considered together. The energy is then redistributed to the streamwise, and especially the spanwise Reynolds stress component, through pressure–strain correlations.

Through visualizations, one-dimensional spectra and two-point correlations, the influence on rotation on turbulence structures is investigated. A distinct unstable side with intense turbulence and vortical structures, and a stable side with much weaker turbulence, develops in the channel with an apparent sharp border between the two sides. If Ro approaches 0.45 the flow at higher Re partly relaminarizes on the stable side of the channel, and oblique turbulent–laminar patterns develop which resemble the oblique band-like structures found in transitional Couette and channel flows at low Reynolds numbers (Duguet *et al.* 2010; Tuckerman *et al.* 2014). It is

quite remarkable that such patterns exist in rotating channel flow at a significantly higher Re. The study by Brethouwer *et al.* (2012) suggests that turbulent–laminar patterns similar to those found in my DNS at $Ro = 0.45$ and $Re = 20\,000$–$31\,600$ also exist at lower Re, but at a lower Ro, and that the patterns most likely have a longer wavelength at lower Re. This implies that the patterns may appear at low Re in DNS of rotating channel flow if very large computational domains are used.

If Ro is raised further in the present DNS, the turbulent fraction of the flow on the stable side goes down, and eventually the flow relaminarizes there. The unstable part of the channel with strong turbulence diminishes in size with Ro, and when the rotation rate is sufficiently high the whole flow becomes laminar. However, as shown by Brethouwer (2016), a linear instability can develop in rapidly rotating channel flows, causing a continuous cycle of turbulent bursts.

The influence of Re is investigated and found to be significant. At fixed Ro, Reynolds stresses are noticeably stronger on the stable side of the channel at higher Re. When $Ro \leqslant 0.9$, the flow is partly or fully turbulent on the stable channel side at higher Re, whereas at lower Re the turbulent fraction of the flow is significantly smaller and the flow tends to relaminarize faster. Therefore, care has to be exercised when drawing general conclusions from lower Reynolds number studies of rotating channel flow. Attention should also be paid to the size of the computational domain, since that may have a significant influence on large-scale structures like roll cells and the relaminarization of the stable channel side.

On the unstable side of the channel, large counter-rotating streamwise roll cells are observed at $Ro = 0.15$ and 0.45. The roll cells become smaller and less noticeable, and eventually disappear if Ro is increased. This trend is stronger at higher Re, since at high Ro the large-scale modes, which are possibly related to roll cells, are larger at lower Re. This suggests that, at low Re, roll cells may exist in a wider Ro range, but note there is yet no way to unambiguously determine if roll cells exist. The spectra also indicate that at lower Ro the unstable channel side is populated by attached eddies, whereas these appear to be absent at higher Ro, indicating that the interaction between the inner and outer layer is weak in rapidly rotating channel flows.

The present case gives some general insights into the effect of rotation on wall-bounded flows. It is also valuable for turbulence modelling since the influence of rotation in turbulence is still difficult to model. Even for large-eddy simulation it could be a demanding case because correctly predicting the relaminarization of rapidly rotating channel flow may pose a challenge.

Acknowledgements

PRACE is acknowledged for the allocation of computing time at the Jülich Supercomputing Centre in Germany for the REFIT project. Computational resources at PDC were made available by SNIC. The author further acknowledges financial support by the Swedish Research Council (grant nos. 621-2013-5784 and 621-2016-03533).

REFERENCES

ADRIAN, R. J. 2007 Hairpin vortex organization in wall turbulence. *Phys. Fluids* **19**, 041301.

AGOSTINI, L. & LESCHZINER, M. 2016 Predicting the response of small-scale near-wall turbulence to large-scale outer motions. *Phys. Fluids* **28**, 015107.

ALVELIUS, K. 1999 Studies of turbulence and its modelling through large eddy- and direct numerical simulations. PhD thesis, Department of Mechanics, KTH, Stockholm, Sweden.

AROLLA, S. K. & DURBIN, P. A. 2013 Modeling rotation and curvature effects within scalar eddy viscosity model framework. *Intl J. Heat Fluid Flow* **39**, 78–89.

BARKLEY, D. & TUCKERMAN, L. S. 2007 Mean flow of turbulent–laminar patterns in plane Couette flow. *J. Fluid Mech.* **576**, 109–137.

BRETHOUWER, G. 2005 The effect of rotation on rapidly sheared homogeneous turbulence and passive scalar transport. Linear theory and direct numerical simulations. *J. Fluid Mech.* **542**, 305–342.

BRETHOUWER, G. 2016 Linear instabilities and recurring bursts of turbulence in rotating channel flow simulations. *Phys. Rev. Fluids* **1**, 054404.

BRETHOUWER, G., DUGUET, Y. & SCHLATTER, P. 2012 Turbulent–laminar coexistence in wall flows with Coriolis, buoyancy or Lorentz forces. *J. Fluid Mech.* **704**, 137–172.

BRETHOUWER, G., SCHLATTER, P., DUGUET, Y., HENNINGSON, D. H. & JOHANSSON, A. V. 2014 Recurrent bursts via linear processes in turbulent environments. *Phys. Rev. Lett.* **112**, 144502.

CHEVALIER, M., SCHLATTER, P., LUNDBLADH, A. & HENNINGSON, D. S. 2007 A pseudo-spectral solver for incompressible boundary layer flows. *Tech. Rep.*, TRITA-MEK 2007:07, KTH Mechanics, Stockholm, Sweden.

CHRISTENSEN, K. T. & ADRIAN, R. J. 2001 Statistical evidence of hairpin vortex packets in wall turbulence. *J. Fluid Mech.* **431**, 433–443.

DAI, Y.-J., HUANG, W.-X. & XU, C.-X. 2016 Effects of Taylor–Görtler vortices on turbulent flows in a spanwise-rotating channel. *Phys. Fluids* **28**, 115104.

DEUSEBIO, E., BRETHOUWER, G., SCHLATTER, P. & LINDBORG, E. 2014 A numerical study of the stratified and unstratified Ekman layer. *J. Fluid Mech.* **755**, 672–704.

DEUSEBIO, E., CAULFIELD, C. P. & TAYLOR, J. R. 2015 The intermittency boundary in stratified plane Couette flow. *J. Fluid Mech.* **781**, 298–329.

DUGUET, Y. & SCHLATTER, P. 2013 Oblique laminar–turbulent interfaces in plane shear flows. *Phys. Rev. Lett.* **110**, 034502.

DUGUET, Y., SCHLATTER, P. & HENNINGSON, D. S. 2010 Formation of turbulent patterns near the onset of transition in plane Couette flow. *J. Fluid Mech.* **650**, 119–129.

GAI, J., XIA, Z., CAI, Q. & CHEN, S. 2016 Turbulent statistics and flow structures in spanwise-rotating turbulent plane Couette flows. *Phys. Rev. Fluids* **1**, 054401.

GARCIA-VILLALBA, M. & DEL ÁLAMO, J. C. 2011 Turbulence modification by stable stratification in channel flow. *Phys. Fluids* **23**, 045104.

GRUNDESTAM, O., WALLIN, S. & JOHANSSON, A. V. 2008 Direct numerical simulations of rotating turbulent channel flow. *J. Fluid Mech.* **598**, 177–199.

HAMBA, F. 2006 The mechanism of zero absolute vorticity state in rotating channel flow. *Phys. Fluids* **18**, 125104.

HSIEH, A. & BIRINGEN, S. 2016 The minimal flow unit in complex turbulent flows. *Phys. Fluids* **28**, 125102.

HSIEH, A., BIRINGEN, S. & KUCALA, A. 2016 Simulation of rotating channel flow with heat transfer: evaluation of closure models. *Trans. ASME J. Turbomach.* **138**, 111009.

HWANG, Y. 2015 Statistical structure of self-sustaining attached eddies in turbulent channel flow. *J. Fluid Mech.* **767**, 254–289.

IIDA, O., FUKUDOME, K., IWATA, T. & NAGANO, Y. 2010 Low Reynolds number effects on rotating turbulent Poiseuille flow. *Phys. Fluids* **22**, 085106.

JAKIRLIĆ, S., HANJALIĆ, K. & TROPEA, C. 2002 Modeling rotating and swirling turbulent flows: a perpetual challenge. *AIAA J.* **40**, 1984–1996.

JEONG, J. & HUSSAIN, F. 1995 On the identification of a vortex. *J. Fluid Mech.* **285**, 69–94.

JOHNSTON, J. P., HALLEEN, R. M. & LEZIUS, D. K. 1972 Effects of spanwise rotation on the structure of two-dimensional fully developed turbulent channel flow. *J. Fluid Mech.* **56**, 533–559.

KAWATA, T. & ALFREDSSON, P. H. 2016 Experiments in rotating plane Couette flow – momentum transport by coherent roll-cell structure and zero-absolute-vorticity state. *J. Fluid Mech.* **791**, 191–213.

KIM, J., MOIN, P. & MOSER, R. 1987 Turbulence statistics in fully developed channel flow at low Reynolds number. *J. Fluid Mech.* **177**, 133–166.

KOMMINAHO, J., LUNDBLADH, A. & JOHANSSON, A. V. 1996 Very large structures in plane turbulent Couette flow. *J. Fluid Mech.* **320**, 259–285.

KRISTOFFERSEN, R. & ANDERSSON, H. I. 1993 Direct simulations of low-Reynolds number turbulent flow in a rotating channel. *J. Fluid Mech.* **256**, 163–197.

LAMBALLAIS, E., LESIEUR, M. & MÉTAIS, O. 1996 Effects of spanwise rotation on the vorticity stretching in transitional and turbulent channel flow. *Intl J. Heat Fluid Flow* **17**, 324–332.

LAMBALLAIS, E., MÉTAIS, O. & LESIEUR, M. 1998 Spectral-dynamic model for large-eddy simulations of turbulent rotating channel flow. *Theor. Comput. Fluid Dyn.* **12**, 149–177.

LEE, M. & MOSER, R. D. 2015 Direct numerical simulation of turbulent channel flow up to $Re_\tau \approx$ 5200. *J. Fluid Mech.* **774**, 395–415.

LENAERS, P., LI, Q., BRETHOUWER, G., SCHLATTER, P. & ÖRLÜ, R. 2012 Rare backflow and extreme wall-normal velocity fluctuations in near-wall turbulence. *Phys. Fluids* **24**, 035110.

LIU, N.-S. & LU, X.-Y. 2007 Direct numerical simulation of spanwise rotating turbulent channel flow with heat transfer. *Intl J. Numer. Meth. Fluids* **53**, 1689–1706.

MARSTORP, L., BRETHOUWER, G., GRUNDESTAM, O. & JOHANSSON, A. V. 2009 Explicit algebraic subgrid stress models with application to rotating channel flow. *J. Fluid Mech.* **639**, 403–432.

MATHIS, R., HUTCHINS, N. & MARUSIC, I. 2009 Large-scale amplitude modulation of the small-scale structures in turbulent boundary layers. *J. Fluid Mech.* **628**, 311–337.

MONTY, J. P., HUTCHINS, N., NG, H. C. H., MARUSIC, I. & CHONG, M. S. 2009 A comparison of turbulent pipe, channel and boundary layer flows. *J. Fluid Mech.* **632**, 431–442.

NAGANO, Y. & HATTORI, H. 2003 Direct numerical simulation and modelling of spanwise rotating channel flow with heat transfer. *J. Turbul.* **4**, 010.

NAKABAYASHI, K. & KITOH, O. 2005 Turbulence characteristics of two-dimensional channel flow with system rotation. *J. Fluid Mech.* **528**, 355–377.

PERRY, A. E. & CHONG, M. S. 1982 On the mechanism of wall turbulence. *J. Fluid Mech.* **119**, 173–217.

SALHI, A. & CAMBON, C. 1997 An analysis of rotating shear flow using linear theory and DNS and LES results. *J. Fluid Mech.* **347**, 171–195.

SCHMID, P. J. & HENNINGSON, D. S. 2001 *Stability and Transition in Shear Flows*, Applied Mathematical Sciences, vol. 142. Springer.

SMIRNOV, P. E. & MENTER, F. R. 2009 Sensitization of the SST turbulence model to rotation and curvature by applying the Spalart–Shur correction. *Trans. ASME J. Turbomach.* **131**, 041010.

SMITS, A. J., MCKEON, B. J. & MARUSIC, I. 2011 High-Reynolds number wall turbulence. *Annu. Rev. Fluid Mech.* **43**, 353–375.

TALLURU, K. M., BAIDYA, R., HUTCHINS, N. & MARUSIC, I. 2014 Amplitude modulation of all three velocity components in turbulent boundary layers. *J. Fluid Mech.* **746**, R1.

TRITTON, D. J. 1992 Stabilization and destablization of turbulent shear flow in a rotating fluid. *J. Fluid Mech.* **241**, 503–523.

TUCKERMAN, L. S., KREILOS, T., SCHROBSDORFF, H., SCHNEIDER, T. M. & GIBSON, J. F. 2014 Turbulent–laminar patterns in plane Poiseuille flow. *Phys. Fluids* **26**, 114103.

WALL, D. P. & NAGATA, M. 2013 Three-dimensional exact coherent states in rotating channel flow. *J. Fluid Mech.* **727**, 533–581.

WALLIN, S., GRUNDESTAM, O. & JOHANSSON, A. V. 2013 Laminarization mechanisms and extreme-amplitude states in rapidly rotating plane channel flow. *J. Fluid Mech.* **730**, 193–219.

XIA, Z., SHI, Y. & CHEN, S. 2016 Direct numerical of turbulent channel flow with spanwise rotation. *J. Fluid Mech.* **788**, 42–56.

YANG, Z. X., CUI, G. X., ZHANG, Z. S. & XU, C. X. 2012 A modified nonlinear sub-grid scale model for large eddy simulation with application to rotating turbulent channel flows. *Phys. Fluids* **24**, 075113.

YANG, Y.-T. & WU, J.-Z. 2012 Channel turbulence with spanwise rotation studied using helical wave decomposition. *J. Fluid Mech.* **692**, 137–152.